Evaluating Large-Eddy Simulations Using Volume Imaging Lidar Data

SHANE D. MAYOR,* GREGORY J. TRIPOLI, AND EDWIN W. ELORANTA

Department of Atmospheric and Oceanic Sciences, University of Wisconsin—Madison, Madison, Wisconsin

ABSTRACT

The authors apply data analysis techniques that demonstrate the power of using volume imaging lidar observations to evaluate several aspects of large-eddy simulations (LESs). They present observations and simulations of an intense and spatially evolving convective boundary layer on 13 January 1998 during the Lake-Induced Convection Experiment (Lake-ICE). To enable comparison of observed and simulated eddy structure, aerosol scattering was estimated from LES output of relative humidity, a passive tracer, and liquid water. Spatial and temporal correlation functions of aerosol structure from horizontal planes reveal the mean and turbulent convective structure. The correlation functions of the observed and simulated aerosol backscatter are presented as a function of altitude and offshore distance. Best-fit ellipses to the closed contours encircling the origin of the correlation functions are used to obtain the mean ellipticity and orientation of the structures. The authors demonstrate that these two parameters are not sensitive to minor changes in the functional relationship between humidity and optical scattering. The lidar-derived mean wind field is used as a reference for evaluating the LES mean flow.

The ellipses from lidar data indicate that structures near the surface tend to be aligned with the mean wind direction, while in the entrainment zone they are aligned perpendicular to the mean wind direction. In the middle of the mixed layer, convective plumes tended to be circular and, therefore, had no preferred orientation at small lags. At longer lags, however, the correlation functions from the middle of the mixed layer show that the observed convective plumes were organized into linear bands oriented perpendicular to the mean wind direction. The perpendicular bands suggest the important role of gravity waves in organizing convective structures. The study shows that the model generates reasonable coherent structures (open cells) where the LES technique is expected to perform poorly (near the surface) and fails to capture the wind-perpendicular organization of closed cells in the middle of the mixed layer where the LES technique is expected to be robust. The authors attribute this failure to the boundary conditions that limited the growth of waves above the mixed layer.

1. Introduction

Large-eddy simulations (LESs) have become a popular tool used to study the atmospheric boundary layer. Most LES experiments are of idealized boundary layers and tests for their accuracy involve comparing turbulence statistics with those from in situ sensors used in the real atmosphere and in laboratory flows. These turbulence statistics are commonly obtained from point measurements on a fixed platform such as a tower or kytoon, or a moving platform such as an airplane. Unfortunately, as shown by Lenschow et al. (1994) and Gluhovsky and Agee (1994), the sampling errors on such measurements are generally much larger than those that can be obtained by using LES output. This is par-

ticularly true for higher-order moments. Moreover, the in situ measurements are not able to show the two- and three-dimensional structure of turbulence that LESs are designed to generate (Stevens and Lenschow 2001).

Active remote sensors, such as radar and lidars, offer an alternative class of measurements that can be used to verify LES. These remote sensors transmit pulses of radio frequency or optical electromagnetic radiation in order to provide an almost instantaneous snapshot of atmospheric conditions along the instrument's line of sight. By redirecting, or scanning, the line of sight in one or two directions, active remote sensors are able to construct two- and three-dimensional images of atmospheric structure.

Unfortunately, aerosol backscatter, a variable obtained from all lidars, is not typically used by modelers for comparison with model output. Furthermore, most lidars provide only relative aerosol backscatter intensity due to the difficulty in making an absolutely calibrated backscatter measurement. Some lidars and radars are capable of providing radial velocity or the concentration of a gas such as water vapor or ozone, but thus far, such instruments are rare, complex, and only beginning to

provide eddy-resolving measurements of those specific variables. Elastic backscatter aerosol lidars, on the other hand, are relatively simple, more common, and provide excellent signal-to-noise ratio data that permit rapid scanning.

Fortunately, LESs are capable of simulating optical scattering of the cloud-free boundary layer if they predict the relative humidity and simulate transport of a passive tracer. For a given air mass with an unchanging mix of aerosol particle types, the magnitude of optical aerosol scattering is mostly a function of the relative humidity and aerosol particle concentration. The absolute magnitude of the optical scattering is not important for determining the turbulence structure. We are interested in the patterns of the inhomogeneities of relative aerosol scattering created by turbulence. Therefore, the objective of this paper is to demonstrate the usefulness of two- and three-dimensional aerosol backscatter lidar data to check mean and turbulence properties of LESs. The techniques we describe supplement other tests of LES performance such as those described by Nieuwstadt et al. (1993), Andren et al. (1994), and Khanna and Brasseur (1997). Although the University of Wisconsin's Nonhydrostatic Modeling System (UW-NMS) was chosen as the LES code for this work, other codes could have been used to demonstrate this main objective.

Uses of aerosol backscatter structure data have been documented in many studies. Eloranta et al. (1975) first used an elastic backscatter lidar to measure the radial component of aerosol motion by cross correlation. Porch and Gillette (1977) showed that optical scattering and horizontal wind speed have similar power spectra based upon fast-response integrating nephelometers and anemometers located 5 m above the surface. Kunkel (1978) showed that the power spectra of lidar aerosol backscatter at high frequency have a $f^{-5/3}$ power-law dependence. Kunkel et al. (1980) used aerosol lidar data to determine turbulence spectra and energy dissipation rates in the boundary layer. Ferrare et al. (1991) used volumetric aerosol lidar data to monitor the evolution of convective structures in a convective boundary layer. Avissar et al. (1998) compared autocorrelation functions of lidar backscatter with simulated aerosol scattering in an LES of a homogeneous convective boundary layer. Therefore, this paper builds upon the previous research and demonstrates how techniques that use aerosol backscatter data can be applied to the testing of LESs of inhomogeneous convective boundary layers.

2. Lidar observations

The University of Wisconsin's volume imaging lidar (VIL) was set up in Sheboygan, Wisconsin, for the Lake-Induced Convection Experiment (Lake-ICE; Kristovich et al. 2000). For more details on the VIL in Lake-ICE, see Mayor and Eloranta (2001, hereafter referred to as ME). The VIL site, located on the western shore of Lake
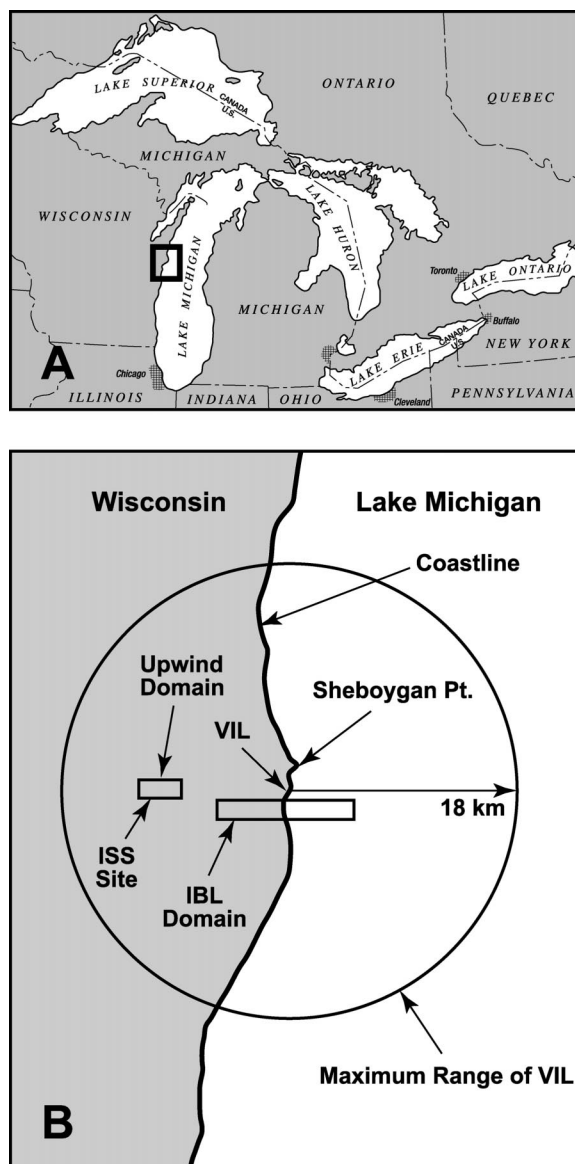

FIG. 1. Location of the VIL during Lake-ICE and relative sizes and positions of LES domains.

Michigan, was selected to observe the leading edge of the intense convective boundary layer that forms over the lake during cold-air outbreaks with westerly and northwesterly flow. The lidar was located in Sheboygan, approximately 2 km south of Sheboygan Point, and within 10 m of Lake Michigan. The shoreline near Sheboygan is aligned roughly north–south. Lake Michigan is approximately 100 km wide at this latitude. The terrain west of Sheboygan is rolling hills covered by forests, farmlands, and small towns. The elevation varies by less than 200 m within 150 km from Sheboygan. Figure 1 shows a map of the region. Outlines of the LES domains are included on this map and will be discussed in section 4.
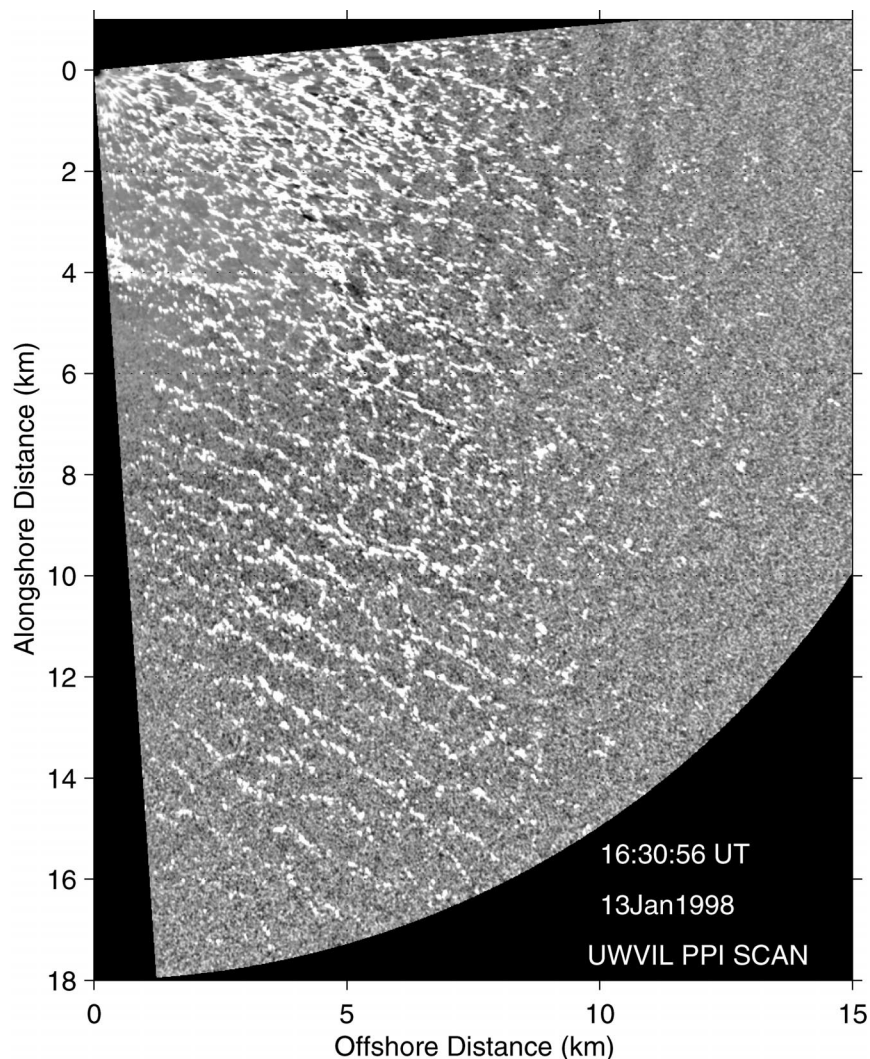
FIG. 2. One PPI scan from the VIL on 13 Jan 1998. A 60-point high-pass median filter has been applied to these data to remove distracting features.

The VIL is an elastic backscatter lidar that transmits at a wavelength of 1064 nm and records backscatter intensity with 15-m resolution out to 18-km range. The laser transmits 400-mJ pulses at a rate of 100 pulses s^{-1}. The duration of each pulse is 3 ns. The wavelength makes it most sensitive to particles that are about 1 μm and larger. Aerosol particles in this size range are abundant in the atmosphere and usually occur in concentrations low enough so that only weak attenuation occurs over distances of several kilometers. Dense water clouds, such as cumulus, severely attenuate the lidar signal.

Bright scattering features such as the densest wisps of steam fog cause harsh and distracting shadows in the lidar data. Often, useful aerosol structure information exists in the shadows but cannot be seen in unfiltered images because the shadow places it beyond the limits of the color scaling, which is usually selected to show

structures in the brighter parts of the image. If not removed, the shadows will also dominate atmospheric structure in the spatial correlation functions. Therefore, a high-pass median filter was applied to each lidar return array after being corrected for a one-over-range-squared dependence. The high-pass median filter subtracts the local median value from each point in the lidar return array.

The VIL is capable of several types of scans. Images of aerosol scattering on an almost-horizontal plane just above the surface of the lake can be obtained from plan-position indicator (PPI) scans. Figure 2 shows a single PPI from 13 January 1998 that took about 12 s to obtain. The PPI scan was created by holding the elevation angle at 0° and changing the azimuth angle at a constant rate. The angular spacing between laser pulses in Fig. 2 was 0.08°. The VIL's beam-steering unit was located 5 m above the surface of the lake. Due to the curvature of
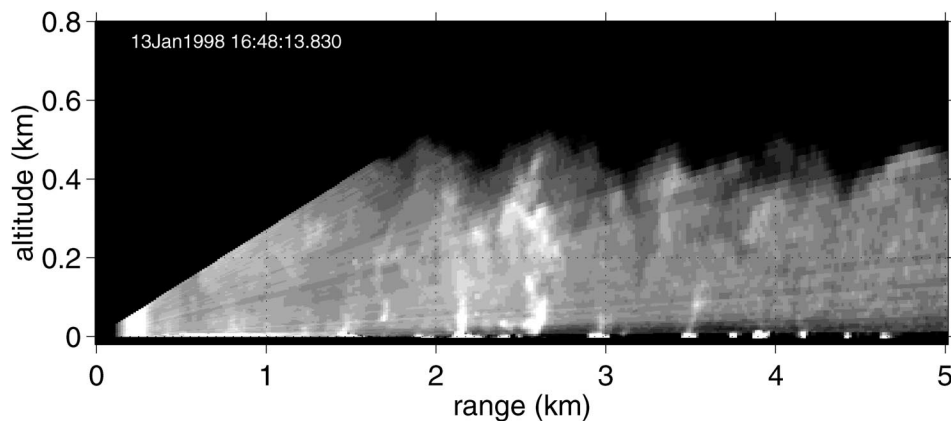
FIG. 3. One RHI scan from the VIL on 13 Jan 1998. (High-pass median filter not applied.)

the earth and atmospheric refraction, we estimate the laser beam to be approximately 12 m above the surface at 10-km range when the lidar is pointing at an elevation angle of 0°. Figure 3 shows a single 0°–15° range–height indicator (RHI) scan from 13 January 1998. Here, the azimuth angle is held constant while the elevation angle is changed. This type of scan takes about 2 s to complete and the angular spacing between laser pulses is 0.26°. This vertical cross section of the mixed layer shows high-scattering patches near the surface associated with steam fog and the walls of the convective cells. Note the image in Fig. 3 is stretched in the vertical. As with all images of scattering intensity shown in this paper, the brightness is proportional to backscatter intensity.

To image the three-dimensional structure of the atmosphere, a series of RHI scans are made, each with an incremented azimuth angle. Such a set of RHIs is called an RHI volume scan. Because the PPI scans and RHI volume scans will be used to infer spatial information, such as eddy shape, it is important to apply a correction for the advection of structures due to the mean horizontal wind during the time required to make a scan. The distortion correction is performed using a procedure described by Sasano et al. (1982) and again by Schols and Eloranta (1992). The data are interpolated from their original spherical coordintes to Cartesian coordinates. Figure 4 is an example of data from one RHI volume scan interpolated to eight horizontal planes. Each horizontal plane is called a constant altitude PPI (CAPPI). In this case, the RHI volume scan consisted of RHIs that ranged from 90° to 130° in azimuth and 0° to 15° in elevation. One such volume scan requires about 2 min to complete. Because of the decorrelating nature of turbulence it is necessary that the time difference between any two points in an image be small compared to the timescale of the flow. Therefore, small-scale features in our images are more accurately imaged than the large-scale features if both large- and small-scale features have the same correlation times. We com-

ment on the implications of this in our conclusions in section 5c.

Strong cold-air outbreaks with westerly flow occurred on several dates during Lake-ICE; however, we chose 13 January for simulation because the weakly convective boundary layer upwind of the lake was limited to 400-m depth and the VIL data contained excellent PPI and RHI scans. The lidar observations on that date show a mixed-layer advecting offshore, ''open cells'' near the surface, and ''closed cells'' in the middle and upper altitudes of the mixed layer. The phrases open cell and closed cell are typically used to describe the organization of mesoscale shallow convection with aspect ratios much larger than those reported here (see, e.g., Atkinson and Zhang 1996). Although the mesoscale and microscale versions of this phenemona are different, we adopt the use of those phrases here because of the similarity in patterns. In both cases, open cells are characterized by high-scattering (cloudy) walls and low-scattering (cloud free) interiors. Closed cells are characterized by low-scattering (cloud free) walls and high-scattering (cloudy) interiors. Closed cells in lidar images resemble popcorn kernels.

PPI scans, such as in Fig. 2, and CAPPIs at altitudes in the surface layer (Fig. 4 top), show a series of interconnected open cells within the first 10 km offshore. These open cells are similar to those observed on 10 and 11 January under similar conditions and are shown in ME and Mayor (2001), respectively. As discussed in ME, the cells are similar to those patterns observed in tank experiments of convection with no mean horizontal flow by Willis and Deardorff (1979) and modeled with LES by Schmidt and Schumann (1989). Intense rising motion is confined to the narrow walls of the cells with weaker subsidence in the cell interior. The CAPPIs (Fig. 4) indicate that this open-cell pattern is confined to the lowest 100 m on all of the 3 days we observed them.

The brightest spots on the CAPPIs at altitudes above about 100 m are circular closed-cell structures rather
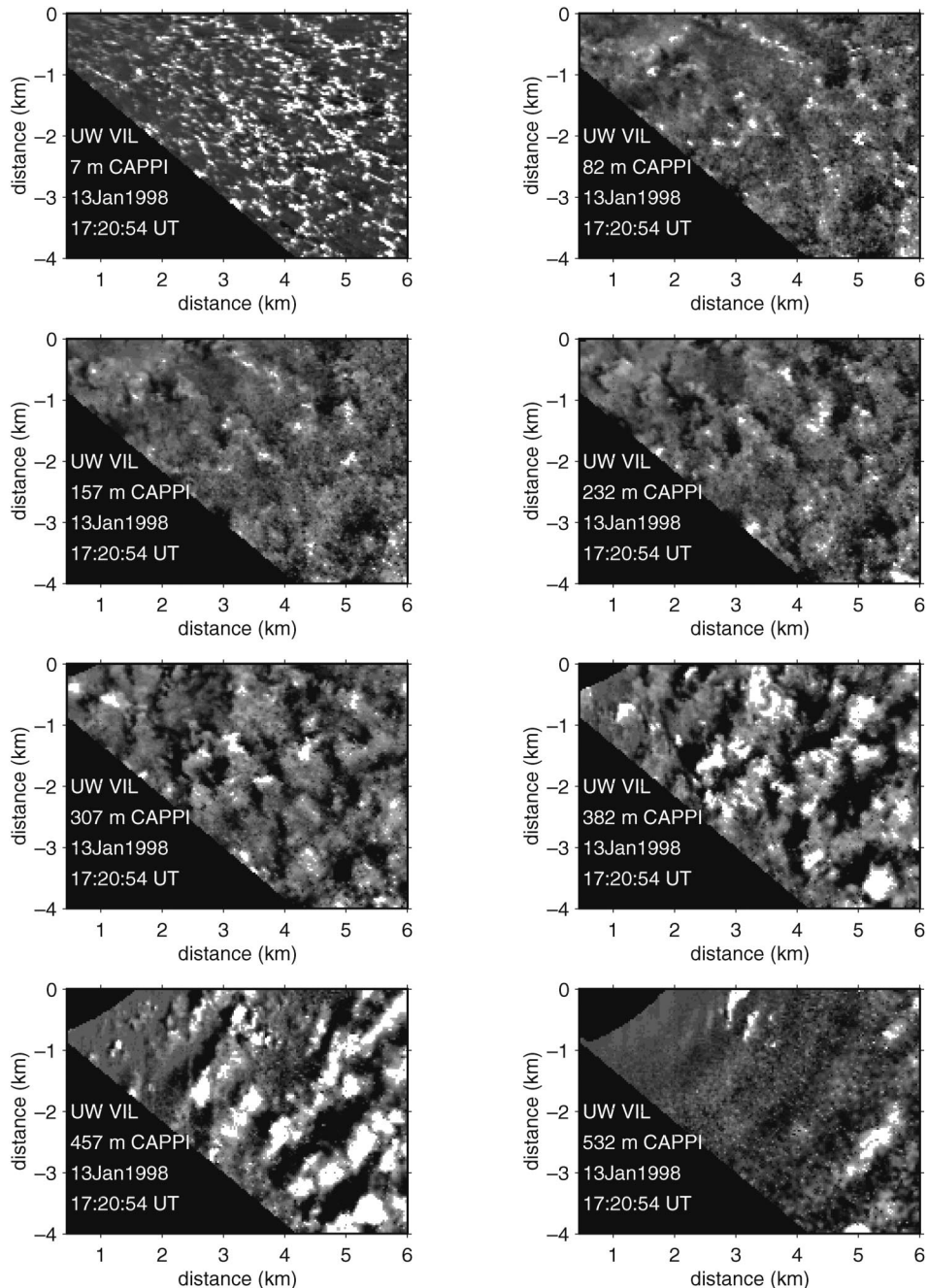
FIG. 4. Eight CAPPIs from one RHI volume scan on 13 Jan 1998. A 60-point high-pass median filter has been applied.

than narrow walls. This closed-cell pattern of convection has been observed many times in other experiments by lidars (see, e.g., Ferrare et al. 1991; Eloranta and Forrest 1992). It is worth noting that the closed cells observed by lidars are the same phenemona that appear as ''open cells'' when observed by high-power weather radars. In clear convective conditions, the radar senses variations in the radio refractive index on the outer edge of the plumes, which therefore result in a cellular-type appearance in radar PPI scans. Konrad (1970) presents excellent examples of this.

3. Simulated lidar aerosol backscatter

Lidar backscatter intensity to first order is dependent upon the concentration of aerosol particles and their size. Aerosol particles swell as the relative humidity (RH) increases. To enable the comparison of model out-
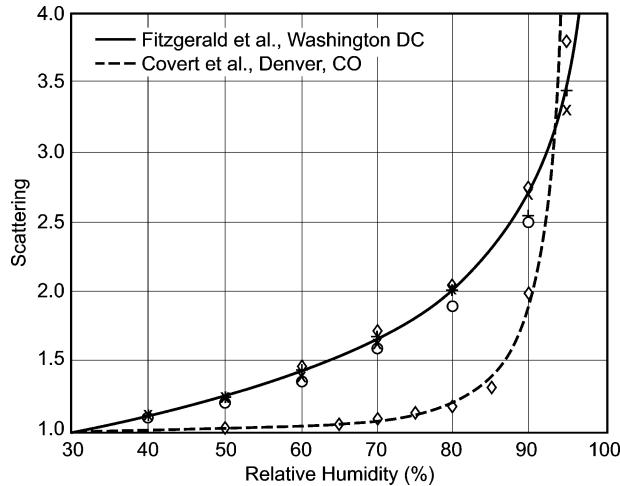
FIG. 5. Optical scattering as a function of relative humidity for data collected by Fitzgerald et al. (1982) (solid line) and Covert et al. (1972) (dashed line).

put with lidar backscatter data, aerosol scattering was simulated by first computing optical scattering (α) relative to the optical scattering at 30% RH from functions that use the RH as the independent variable (see Fig. 5). Unfortunately, aerosol particle types change with time and location, and observations to show the functional relationship between RH and α were not collected during our field experiment. Therefore, we have used data, published in two other papers, that represent extreme cases. Data from Fitzgerald et al. (1982) were collected during the summer in Washington, D.C., and data from Covert et al. (1972) were collected in October in Denver, Colorado. In section 5g we show that characteristics of LES eddy structure such as ellipticity and orientation are insensitive to the choice of these curves. The best-fit functions to the Fitzgerald and Covert data are given by

$$\alpha = -2.5 + \frac{8.4}{(100 - \text{RH})^2} \quad \text{and} \quad (1)$$

$$\alpha = -0.98 + \frac{117.92}{(100 - \text{RH})^2}, \quad (2)$$

respectively.

To avoid the very unrealistic infinite scattering when the relative humidity is at or above 100%, all occurrences of model relative humidity greater than 99.99% are set to 99.99%. Furthermore, if any liquid water is found at a grid cell, the simulated aerosol scattering at that location is assigned a value of optical scattering for a relative humidity of 99.99%. For the fit to the Fitzgerald et al. data, the optical scattering at 99.99% is equal to 18.5 times that at 30%. For the fit to the Covert et al. data that value is 1.8×10^6 times that at 30%. We attempt to include the effect of steam fog cloud droplets because even a few relatively large cloud drop-

lets produce tremendous optical scattering when compared to the scattering by many small aerosol particles.

To obtain simulated lidar scattering, the optical scattering from either Eq. (1) or (2) is multiplied by a model passive tracer. The passive tracer is initialized as one below 400 m and zero above 400 m. Therefore, where no passive tracer is present, such as above 400 m, the simulated lidar scattering is zero. During the simulation the mixed layer entrains the tracer-free air from air above it resulting in the formation of small inhomogeneities in the passive tracer concentration in the mixed layer. Finally, we take the log of the simulated lidar scattering to mimic the effect of the VIL's log amplifier.

4. Large-eddy simulations

We chose UW-NMS (Tripoli 1992) as the LES code in our work because it was convenient and it supported nonperiodic boundary conditions. LES of a mesoscale internal boundary layer (IBL) using a stationary grid requires using either nested grids or open-downstream and closed-upstream boundary conditions. Early in our research, we chose the later method and have described it completely in Mayor et al. (2002). Our first attempts at simulating the 13 January IBL using that general method are presented in Mayor et al. (1999). These early simulations used a domain that was entirely over water and resulted in a nonmoving shore-parallel band of steam fog immediately downstream of the inflow wall because of the lack of eddies there (see Fig. 6a). As convection developed in the simulation, inhomogeneities were observed along the downstream edge of this fixed band of fog. This result, when compared with the lidar observations, clearly demonstrated the need to include turbulent flow over the land in the simulations to capture a more natural transition immediately downstream of the shore. Therefore, we began running substantially larger domains that included a section over land upwind of the section over the lake.

Eventually, a three-dimensional rectangular domain consisting of 779 × 120 × 69 grid points with 15-m spacing in all three directions was chosen. A time step of 0.5 s was used. The size of the domain was 11.68 km by 1.8 km by 1 km tall. The western 400 grid points (6 km) were over land and the eastern 379 grid points (5.68 km) over water. This provided a modest and inadequate region upstream of the lake for eddies to develop. (This long rectangular domain is shown in Fig. 1b to indicate the size of the domain relative to coastline curvature and maximum range of the lidar.) In order to generate fully developed, homogeneous, and stationary turbulence over the land side of the model domain, a perturbation recycling method was adopted based on the work of Lund et al. (1998) and originally inspired by that of Spalart (1988). A detailed description of the initialization and boundary conditions used in the simulations is presented in Mayor et al. (2002).

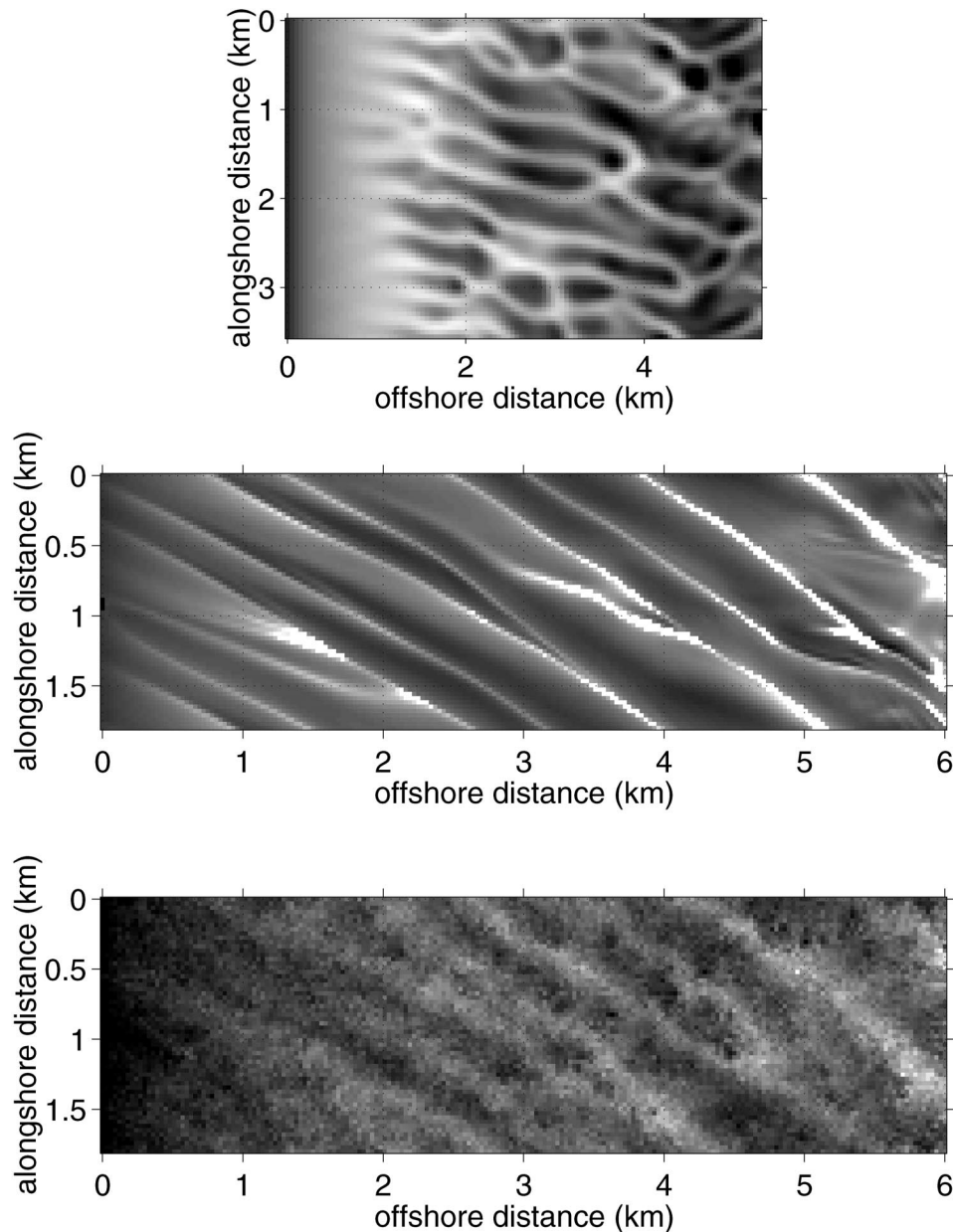It is desirable for the LES to resolve scales observable

FIG. 6. Examples of LES solutions (snapshots of simulated lidar scattering) on horizontal planes at 7.5 m above the surface that were clearly incorrect when compared with lidar observations. (top) The lack of turbulent structures at the shore results in a shore-parallel, homogeneous band of steam/fog. (middle) Almost nonmoving linear wind-parallel bands result from a nondimensional mixing coefficient that is too large. (bottom) All coherent structures are eliminated by noise when the nondimensional mixing coefficient is set to zero.

by the lidar (15 m); however, that requires more computer resources than were available at the time of this study. To simulate the smallest-scale features observable by the lidar with sufficient accuracy, a second-order finite-difference scheme, such as the one used in our LES, would require grid spacing of no more than 2.5 m. A second desirable characteristic of grid spacing was to use a value that was an integer multiple of the lidar data spacing in order to eliminate interpolation and fa-

cilitate ease in comparison. Therefore, we selected 15-m grid spacing and set the domain in the vertical so that the lowest velocity point in the atmosphere was 7.5 m above the surface, an ideal altitude for comparison with data from the VIL's 0° elevation PPI scans. VIL CAPPIs were also constructed starting at 7.5 m AGL to facilitate comparison with model output.

The LES technique in general is not expected to perform well at the lowest grid point due to the presence

TABLE 1. Some of the simulations discussed.

Run name	Advection scheme	c
ENST	Enstrophy conserving	0.05
CNTRL	Enstrophy nonconserving	0.05
DIFF	Enstrophy nonconserving	0.15

of the surface and the large role of the subgrid-scale (SGS) model in such locations. However, our model output at the lowest grid levels shows cellular structures with horizontal scales that are approximately the depth of the mixed layer. Similar patterns are seen in LES output at 0.25 z/z_i by Schmidt and Schumann (1989) and 0.05 z/z_i by Mason (1989). Willis and Deardorff (1979) show similar patterns occurring ''very near the lower surface'' in a tank experiment. The cellular structures are remarkably similar to those observed by the lidar and are evidence that the largest, and most well-resolved, eddies of this particular flow have a strong effect on the patterns close to the surface. For the LES results presented here, numerical filters and eddy viscosity limit the effective resolving capability of the model to approximately 5–6 times the grid spacing. The filters and eddy viscosity have a larger effect on the smallest scales ($2\Delta x$) and become less effective for larger scales (5–$6\Delta x$). This means that eddies smaller than about 90 m are not entirely explicitly simulated. For scales greater than about 90 m the features are entirely resolved.

To demonstrate how the lidar data can be used to discriminate among several different, yet reasonable, model solutions we sought a model parameter that would result in different simulated flow characteristic when changed. The nondimensional mixing coefficient c was chosen. In our code, it is used with the grid-spacing l and the square root of the eddy kinetic energy e to obtain the eddy viscosity K_m:

$$K_m = cl\sqrt{e}. \tag{3}$$

We found that when c is approximately equal to or greater than 0.20, the model converges to an almost constant solution after running for longer than approximately 2 h (shown in Fig. 6b). As c is decreased, more temporal and spatial variation can be seen in the solutions. When $c = 0$, noise prevents the simulation from developing coherent structures (see Fig. 6c).

For our tests, summarized in Table 1, we ran two IBL simulations with $c = 0.05$ and one with $c = 0.15$. One of the simulations (ENST) used an enstrophy conserving advection scheme and two simulations (CNTRL and DIFF) did not. The convective patterns for all three cases are very similar and, for brevity, we only show a solution to one of them (ENST) in Fig. 7. This figure shows simulated lidar scattering over the water only (the
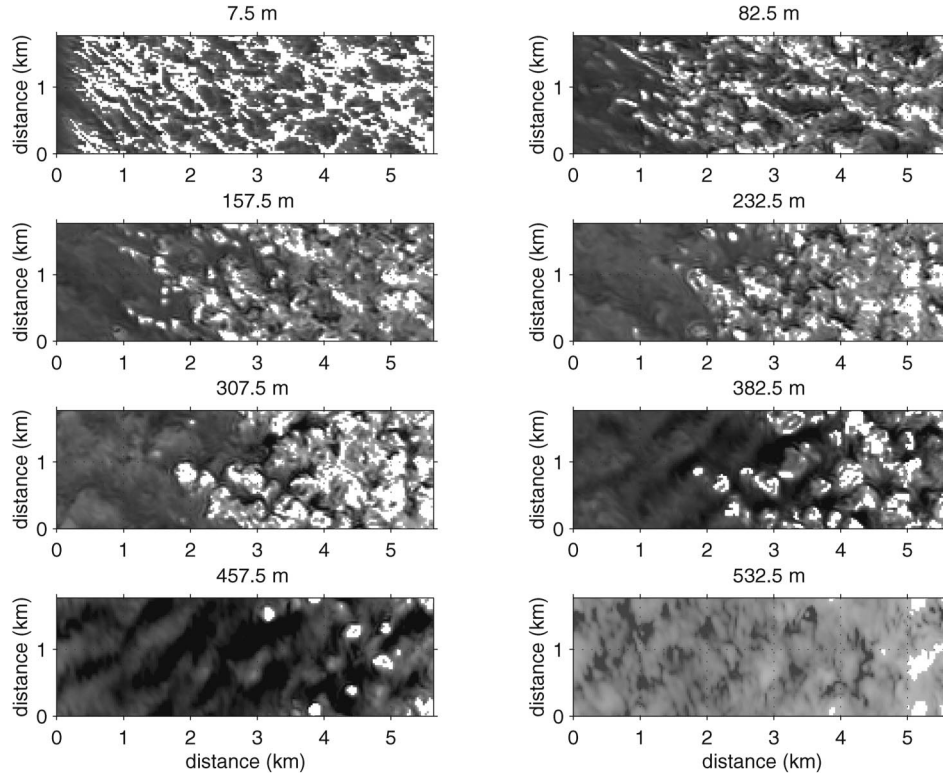

FIG. 7. Simulated lidar aerosol scattering on horizontal planes at eight altitudes over the lake in the LES. The eight altitudes were chosen to match those in Fig. 4.
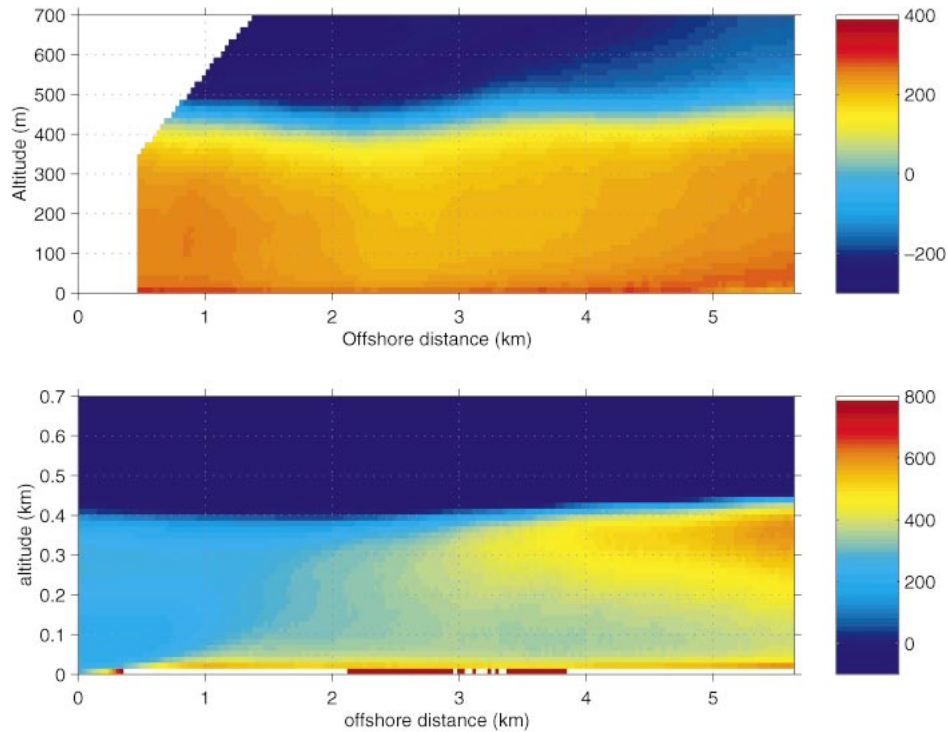
FIG. 8. Observed mean aerosol scattering as a function of offshore distance and altitude from (top) the lidar and the same from (bottom) the simulated lidar aerosol scattering in the LES.

part of the domain over land was omitted in this figure) on horizontal planes for altitudes matching those shown in Fig. 4. Each of the three simulations listed in Table 1 produces patterns with open-cell character near the surface and closed-cell character above about 100 m as discussed at the end of section 2. However, as we will discuss in section 5d, the lidar-derived winds are used to show that the choice of advection scheme does have an effect on the acceleration of the offshore flow.

5. Comparisons

a. Mean aerosol structure

In this short section we present mean aerosol fields on east–west vertical planes from the lidar data and simulation output to show that there is no step change to define the top edge of the IBL when the data and model output are averaged over time. It is important to keep in mind that the boundary layer upwind of the shore was weakly convective, and therefore the IBL here is an intensification of convection rather than a transition from laminar to turbulent flow. Figure 8 shows the mean observed and simulated aerosol scattering as a function of altitude and offshore distance. Both the lidar data and the simulation show a gradual increase in the mean aerosol scattering in the middle of the boundary layer as the offshore distance increases. We also see a slight dip in the top of the mixed layer in Fig. 8. This dip is the

result of divergent flow that was both observed by the lidar and captured in the simulations.

b. Mean wind

The observed mean wind field, derived from cross correlation of the lidar data, is completely described in ME. The cross-correlation technique was applied to the simulated lidar data at the 7.5-m level and the coherent structure motion matches the model winds to within 0.5 m s^{-1} and shows no evidence of bias toward higher or lower speeds. All of the simulations produce a sharp increase in the near-surface wind speed with increasing offshore distance that is more similar to the mean lidar-derived acceleration on 10 January than for 13 January (Fig. 9, top). The lidar-derived wind speed increase for 13 January is much less, probably because most of the lidar sample region appears to lie within a mesoscale eddy associated with Sheboygan Point (see Fig. 11 of ME). The lidar-derived wind field on 10 January (see Fig. 4 of ME) is much less spatially variable than that on 13 January, and the acceleration more similar to that of the model despite the fact that the mean flow is from a slightly different direction. We did not attempt to include shoreline shape or topography in the simulations. The amount of increase in wind speed in ENST is about 3.4 m s^{-1} and it occurs within about 2 km of the shore. A wind speed increase of 4.4 m s^{-1} occurs within the first 4 km for CNTRL and DIFF.
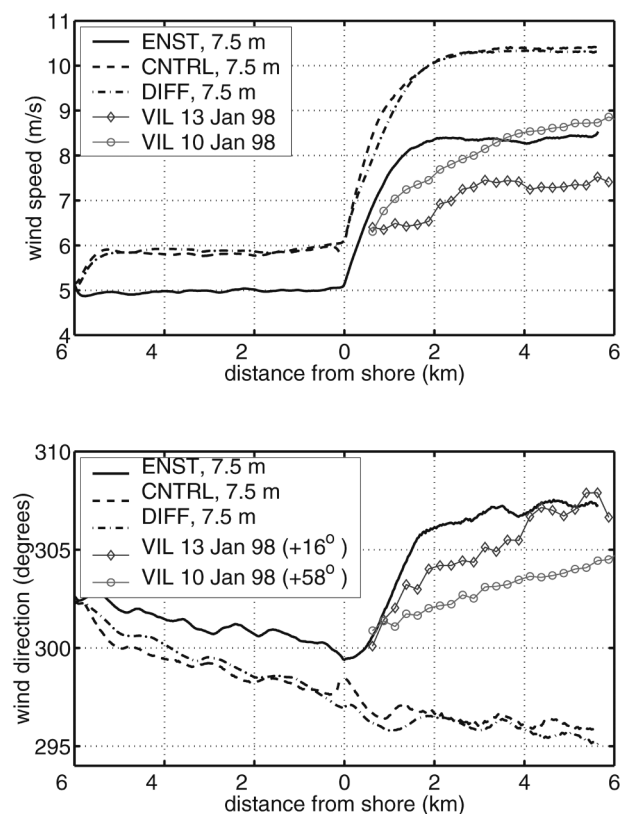
FIG. 9. (top) Wind speed and (bottom) wind direction in the surface layer as a function of distance from the shore from lidar observations and three difference LES runs.

Figure 9 also shows some significant differences in wind direction among the three simulations. In the lower panel, we see that the LES surface layer winds for ENST turn clockwise with increasing offshore distance and counterclockwise in CNTRL and DIFF. The lidar-derived wind direction on 10 and 13 January turn clockwise, although at a smaller rate. This veering of the wind is consistent with the change that would occur to the resulting wind vector in a body force diagram if the friction vector were reduced.

c. Mean horizontal eddy structure

To obtain the mean horizontal eddy structure, we computed two-dimensional correlation functions (CFs) following a procedure described in the appendix. For the lidar data, the range-corrected RHI volume scan data were high-pass median filtered, corrected for distortion, and then interpolated onto a 3D Cartesian grid so that the technique could be applied to data on horizontal planes at multiple altitudes. The CFs were computed for a series of offshore distances and altitudes. For the lidar CFs, the closest offshore distance of the zero lag was 1.77 km and the farthest was 4.65 km. The computations were made at intervals of 360 m. The CFs were computed for a series of altitudes at 30-m intervals ranging

between 7 and 577 m above the surface. Each CF was computed using 30-m lags up to 1 km in both directions and resulting in a two-dimensional array containing 5041 points (71 by 71). The CFs were averaged over time to reduce noise. For the lidar data, this means averaging CFs that were computed from a sequence of RHI volume scans separated in time by 2–3 min. Twenty-seven volume scans were collected during a 78-min period. The CFs of simulated lidar scattering at 12-s intervals were averaged over 30-min periods.

In the appendix (Fig. A2) an example of one CF for ±200 m range of lag is shown. To show many CFs simultaneously, we created Figs. 10 (from lidar) and 11 (from ENST). These figures show many CFs in the offshore and vertical directions. Each small square tile is a CF with ±1 km range of lags and the zero lag, or origin, is located at the center of each tile. This form of presentation tends to emphasize the structure at longer lags, which takes up more area on each CF, and shows how the CFs change as a function of offshore distance and altitude. Figure 10 shows the CFs for the lidar RHI volume scans that were collected during the period from 1719 to 1837 UTC. Figure 11 shows the CFs for ENST from the time period between 1800 and 1830 UTC. Perhaps the most interesting feature in Fig. 10 is the presence of ridges that run through the origin from the lower left to the upper right within 3 km of the shore and below 200-m altitude. Those ridges do not appear at equivalent locations in Fig. 11. The presence of this feature in the lidar data is an indication of lineal structures that are oriented perpendicular to the direction of the mean flow. A closer look at those tiles in Fig. 10 shows that the correlation functions are positive in the extreme upper-left and lower-right corners of those tiles. This is evidence that the lineal features have a wavelength of over 1 km. This organization of convection in the boundary layer may be caused by gravity waves in the capping inversion layer that influence the development of convective plumes beneath them. This may happen by gravity waves changing the height of the capping inversion slightly and, thereby, affecting mean vertical motion and convergence/divergence patterns in the boundary layer with the same spacing as the waves (Hauf and Clark 1989). Animations of PPI scans from 14 December 1997 and 19 January 1998 provide additional observational evidence that waves strongly influence boundary layer turbulence structure.

The absence of the effects of waves in this region in earlier volume scan data (not shown) and their absence at farther ranges are convincing evidence that they are not systematic measurement errors. The absence of the effects of waves in this region in the LES output suggests that the model is not generating sufficient wave energy in the capping inversion. This is most likely a result of the limited domain size and chosen boundary conditions. For example, a taller model domain would have allowed us to move the damping layer higher above the capping inversion, thereby allow wave energy in the
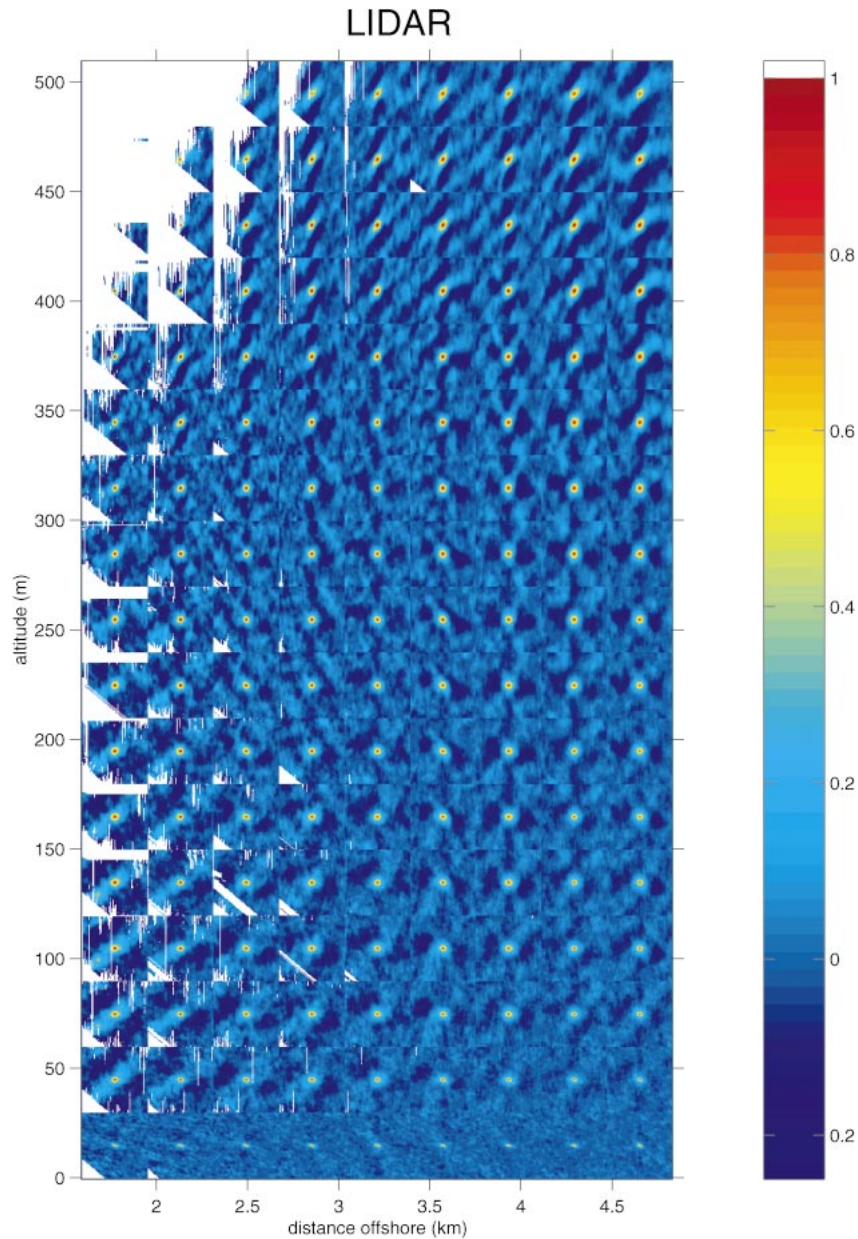
LIDAR

FIG. 10. The 2D horizontal CFs for nine offshore distances and 20 altitudes for the RHI
volume scan data (CAPPIs) collected between 1719 and 1837 UTC 13 Jan 1998.

inversion layer to increase. Another likely cause of reduced wave motion in the simulation is the use of a fixed-inflow boundary condition, which prevents upstream wave propagation.

Figure 11 also shows the tendency for the LES to generate linear structures that are oriented parallel to the wind direction throughout most of the boundary layer. Particularly between 50- and 250-m altitude and from the shore to about 1.5 km offshore, strong flow-parallel bands with 1-km spacing are observed. The effect of increased convective forcing from the lake can be seen in a zone that rapidly deepens to about 200-m

altitude at 2 km offshore. In this region, the band spacing is about 250 m. Some evidence for gravity wave activity exists in the CFs above about 300 m. These CFs have flow-perpendicular bands with spacing of about 250 m.

Based on the inspection of many CFs in this and previous studies it appears that there are two particularly interesting regions on each CF: 1) a steeply sloped region near the origin and 2) the remaining broad region outside the steeply sloped region. The origin of a normalized correlation function is always equal to one, and the CF decreases rapidly as the lag (the distance from the origin) increases. For the lidar CFs on 13 January,
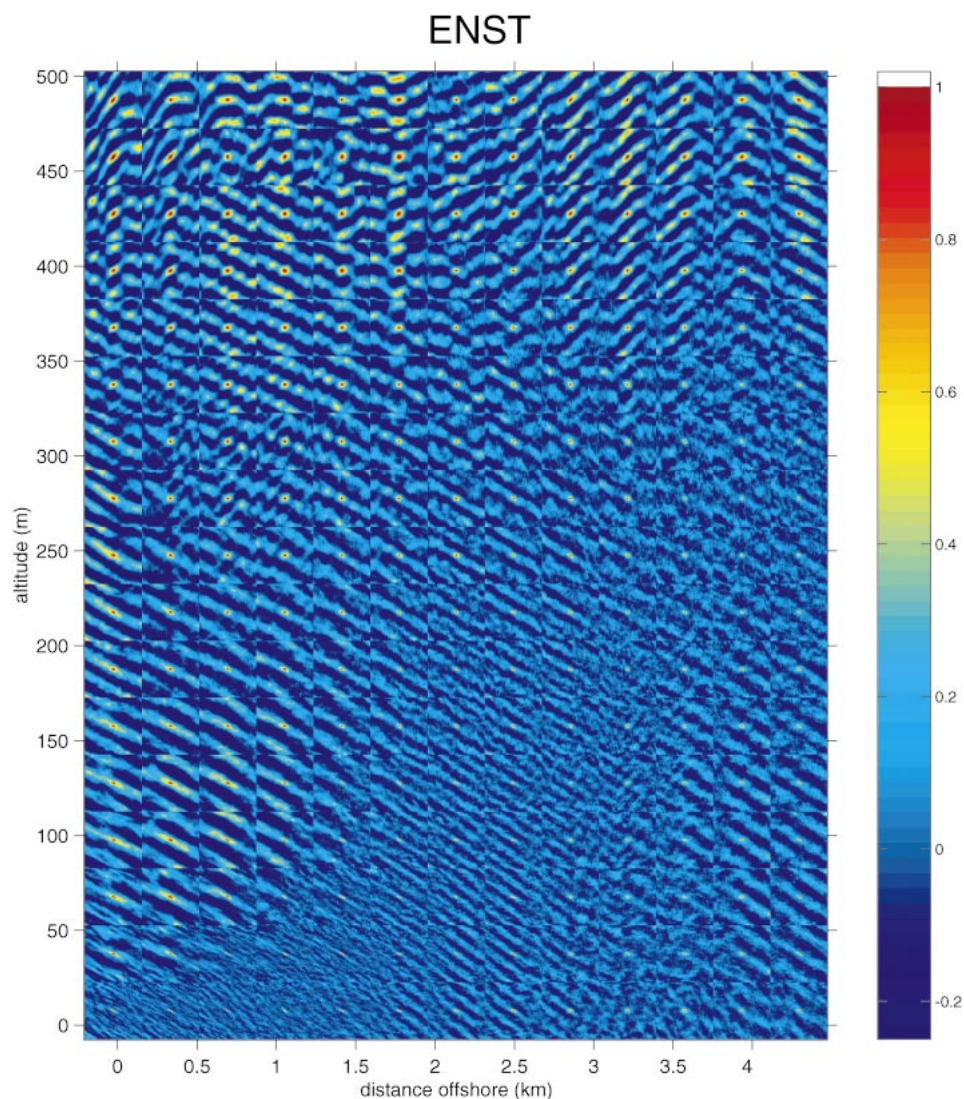
ENST

FIG. 11. The 2D horizontal CFs for 13 offshore distances and 17 altitudes from ENST. These CFs used simulated aerosol scattering on horizontal planes in LES output for the time from 1800 to 1830 UTC.

this rapid decrease occurs within a distance of about 400 m from the origin, which is the same as the depth of the boundary layer on that day. In this region, where the correlation function tends to be greater than about 0.1, a given isopleth of correlation tends to form closed circles and ellipses that change size, shape, and orientation as the offshore distance and altitude change. Small lags on the correlation function correspond to high frequency in power spectra. Therefore, this steep inertial subrange region near the peak can be associated with the cascade of the turbulent kinetic energy of the flow. However, the region very near the origin is also sensitive to small-scale correlation due to linear interpolation in the conversion of data from spherical to Cartesian coordinates. This effect will be discussed in section 5f.

The second interesting region on the CFs is for lags greater than the boundary layer depth and the inertial sub-

range. In this broad region, the isopleths of correlation tend not to form closed contours around the origin. In this region, we can see the effects of mesoscale organization such as horizontal convective rolls. The spacing of lineal rolls can be obtained by determining the distance between the origin and the next local maximum associated with a ridge line that runs approximately parallel to the direction of the flow or the flow's mean shear vector. Because each volume scan take approximately 2 min to complete, large-scale features on CAPPI images contain some distortion due to the decorrelating nature of turbulence. Therefore, we underestimate the magnitude of the correlation function at long lags.

d. Ellipses

Contour levels of 0.1 and above on the 2D CFs tend to form circles or ellipses and lie within the steeply
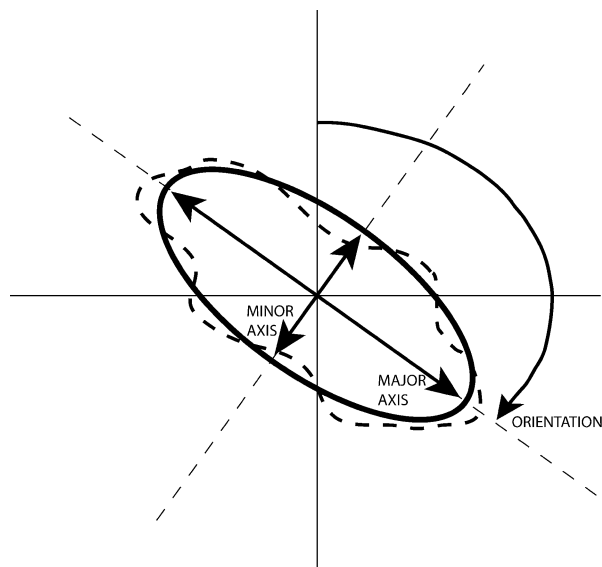
FIG. 12. Diagram showing a best-fit ellipse (solid) to a closed contour (dashed) of a correlation function and the major and minor axes and orientation of the best-fit ellipse.

sloped region. Ellipses can be completely described by three values: major axis length, minor axis length, and orientation (see Fig. 12). The ratio of the major to minor axes is the ellipticity. Near the surface it is common to see ellipticities ranging from 2 to 3. At higher altitudes, the ellipticities decrease, especially offshore where the convection is more intense. Above the boundary layer, where there is no aerosol structure in the lidar data, the ellipses become very small as expected for noise. The best-fit ellipse from a least squares solution to any closed contour encircling the origin of the correlation function

was obtained using functions developed by Gander et al. (1994).

Features such as ellipticity of the contours in the steeply sloped region and periodic linear structures in the broad and generally flat region were shown by Ferrare et al. (1991) using PPI scan data of homogeneous convective boundary layers collected in 1983. They found the orientation of the ellipses to be approximately parallel to the shear vector. Improvements in lidar scanning speed since that time have enabled RHI volume scans as described in the section 2. Therefore, the lidar data can now be used to search for changes in eddy structure as a function of altitude and offshore distance.

The spatial variations of the closed CF contours at the 0.1, 0.2, and 0.3 levels on 13 January are shown in Fig. 13. Some features in this figure, which are common in equivalent presentations from lidar data on other dates and times (not shown), are

1) the gradual increase in size of circles with increase in altitude and a sudden decrease in their size above the BL,
2) the absence of closed contours for some regions near the shore and at higher altitudes,
3) the orientation of the major axes of the ellipses near the surface are aligned approximately parallel to the wind direction while the major axes of the ellipses near the top of the mixed layer (ML) are perpendicular to the mean wind direction, and
4) the lower the contour level chosen, the noisier the appearance of the closed contours.

The increase of area enclosed by a closed contour with altitude in the surface layer suggests that the size of eddies near the surface is restricted by their distance
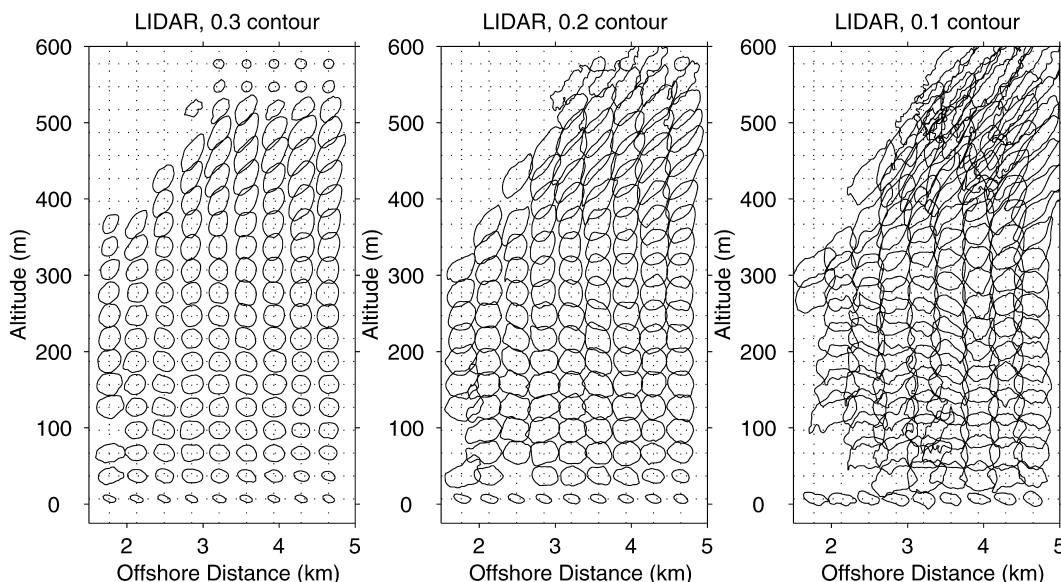

FIG. 13. Contours of (left) 0.3, (middle) 0.2, and (right) 0.1 from CFs of aerosol backscatter data collected between 1719 and 1837 UTC 13 Jan 1998.
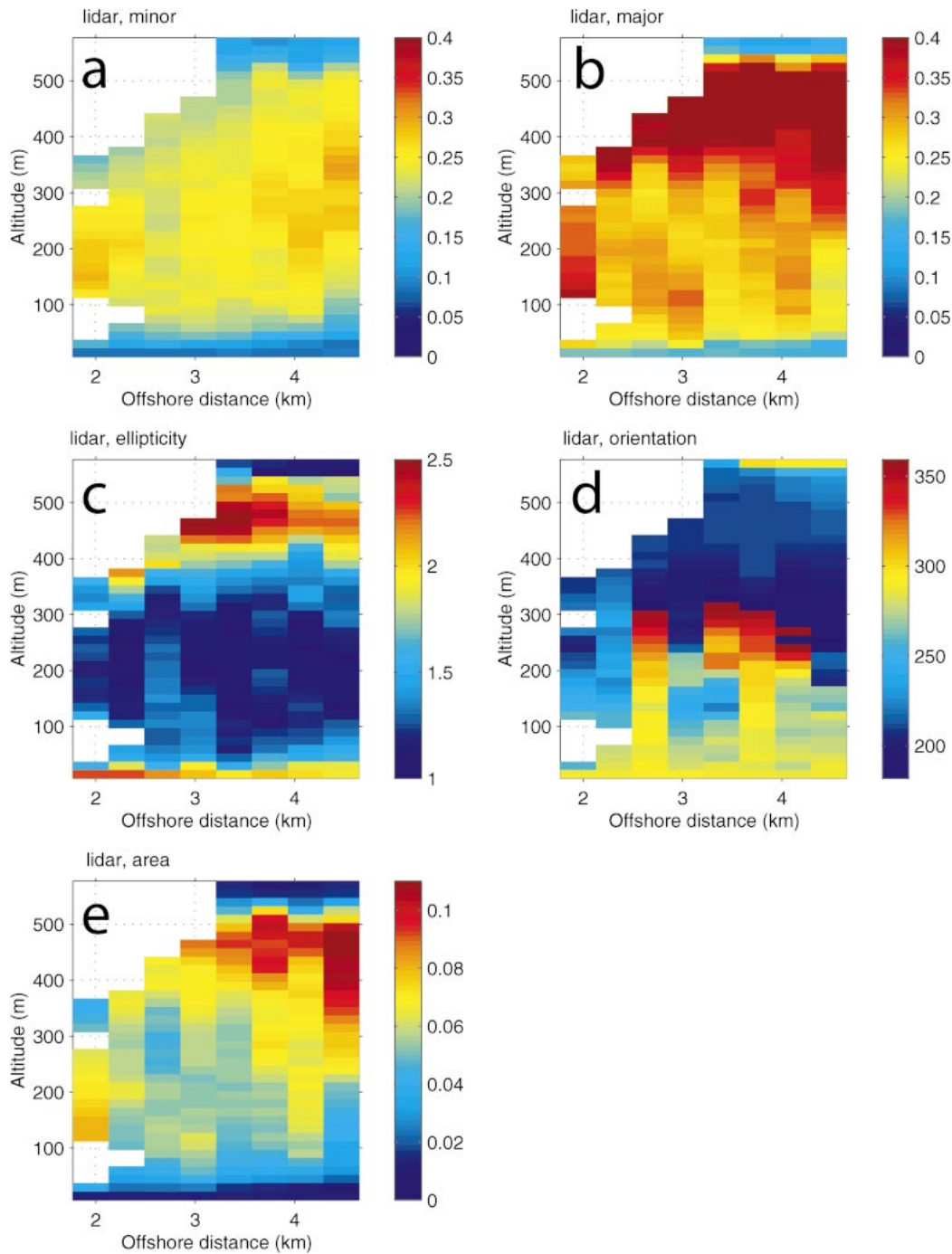
FIG. 14. Quantities derived from ellipses fit to isopleths of 0.3 correlation on CFs from CAPPIs from 1719 to 1837 UTC 13 Jan 1998.

from the surface. The sudden decrease in area enclosed by the contours above the mixed layer is caused by a low signal-to-noise ratio in the relatively clean free troposphere. The regions with no contours indicate that either a closed contour encircling the origin could not be located for the chosen level of correlation or there

was insufficient variability in the lidar data to compute correlation functions.

Figures 14 (from observations) and 15 (from ENST) show best-fit ellipse parameters in image form as a function of offshore distance and altitude. Panels a and b in each figure show the length of the minor and major axes
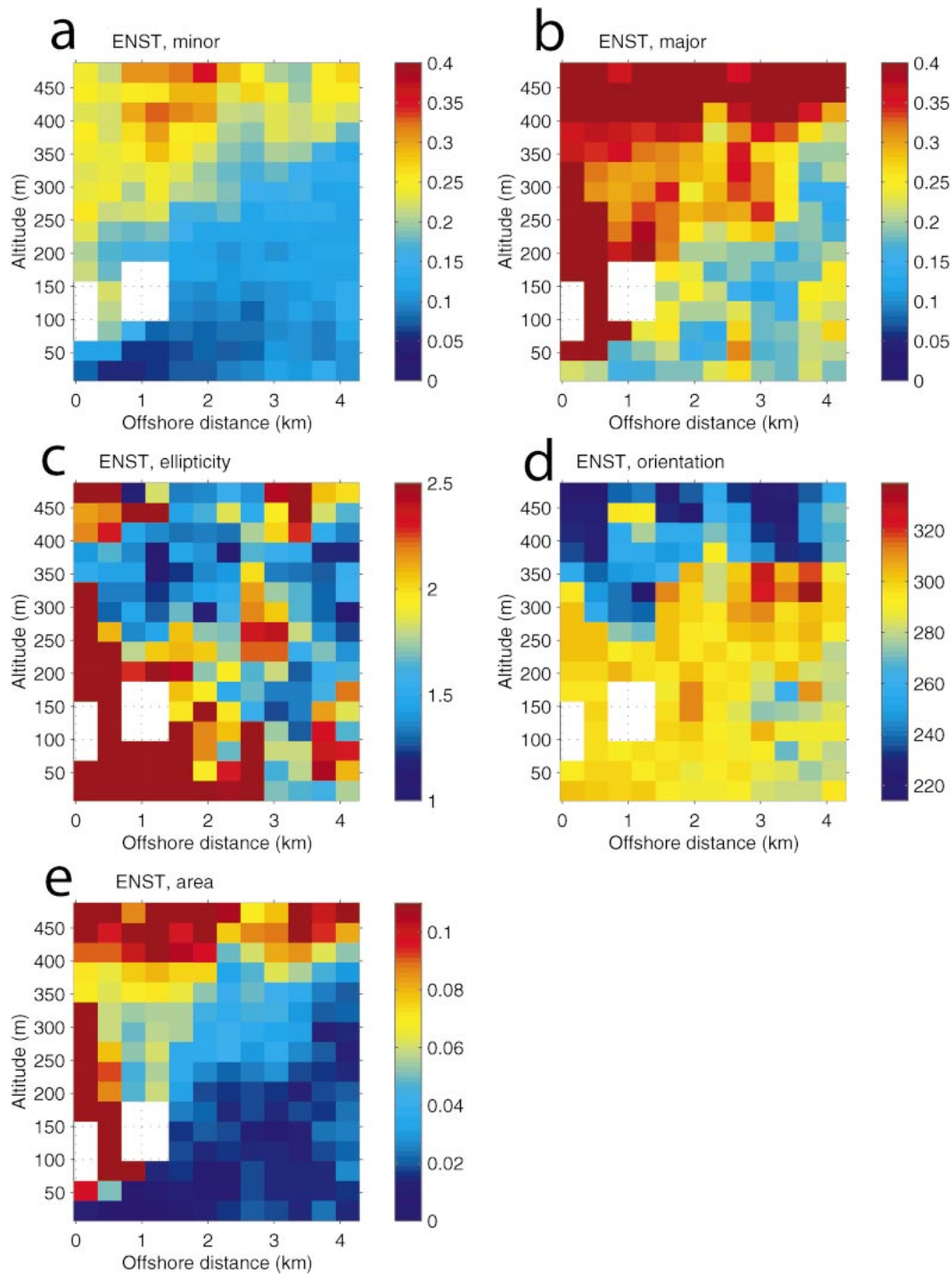
FIG. 15. Quantities derived from ellipses fit to isopleths of 0.3 correlation on CFs from simulated lidar scattering on horizontal planes in ENST.

(km). Panels c and d show the ellipticity and the orientation of the ellipses. Near the surface, where the ellipticity is much greater than 1, we see that the orientations are approximately aligned with the mean wind direction (290°). The area of the ellipses is plotted in panel e in both figures. Figure 14c indicates that there is a slight increase in the

depth of the shallow layer of high ellipticity near the surface with increasing offshore distance.

Figure 16 *appears* to indicate that ENST produced eddies that have larger spatial decorrelation (smaller ellipses) than those observed by the lidar over a very broad range of altitudes in the middle of the IBL. The
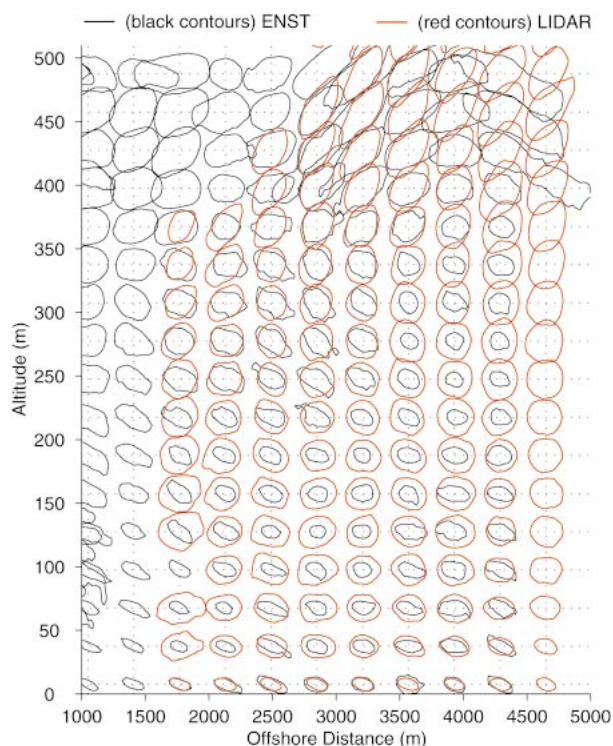
FIG. 16. Comparison of the 0.30 isopleth of correlation on CFs from ENST (black contours) and RHI volume scan data collected between 1719 and 1837 UTC (red contours).

areas enclosed by the contours compare well near the surface and in the entrainment zone. This is also true for CNTRL and ENST. However, as we will show in section 5g, this comparison of ellipse areas from observations and simulations is compromised because the exact optical scattering function was not known during our experiment.

Despite the evidence for horizontal inhomogeneity, such as acceleration of the flow and the intensification of convective plumes with offshore distance, the ellipses change only very slightly as offshore distance increases in this region. Therefore, to summarize the vertical variation of the ellipse parameters, we have averaged the ellipse parameters in the horizontal between 2.85 and 4.29 km offshore. They are shown as a function of altitude in Fig. 17. The error bars represent one standard deviation in each direction for the ellipse parameters for five offshore distances.

Figures 17d and 17b show the minor and major axis lengths as a function of altitude. They show that the observed minor axis lengths are at least a factor of 2 larger than those from the simulation in the middle of the mixed layer. The observed major axis lengths are approximately 50% larger than those from the simulation. The ellipticities are plotted as a function of altitude in the middle-left panel of Fig. 17. They show that near the surface the correlation functions are elongated in the streamwise direction by a factor of 2 more than in the

cross-stream direction. In the middle of the mixed layer, the observed ellipticities are near one. The ellipticities from the simulation are much larger that those from the observations at all altitudes except near the surface, where they appear to decrease slightly. Figure 17d shows the orientation of the best-fit ellipses as a function of altitude. It shows that, near the surface and in the lower mixed layer, the ellipses from both the observations and simulations are aligned with the wind direction. In the middle of the mixed layer, where the ellipticities are near one, subtle changes in the major and minor axis lengths can cause the orientations to change by 90°. Above the mixed layer the observed orientations are clearly about 90° different than the orientations in the middle and lower mixed layer. The orientations from the simulations appear to change in this region but not as sharply as those from the observations. Last, the lower-left panel in Fig. 17 shows the area of the ellipses as a function of altitude. We discuss the reasons for the differences in ellipse areas in section 5g.

e. Effect of high-pass filter length

To test the effect of the high-pass median filter length on the CFs, five high-pass median filter lengths (60, 50, 40, 30, and 20 points) were applied to the series of volume scans collected between 1719 and 1837 UTC on 13 January. A casual inspection of the image shows no noticeable differences in the images with these various filter lengths. However, the median filter length does have an effect on the CFs above the lowest levels as shown in Fig. 18.

In Fig. 18, contours for all median filter lengths are approximately the same size for the 7.5-m level. This indicates that the variability occurs on scales smaller than the shortest median filter (300 m). At altitudes above 7.5 m, however, the smaller median filter lengths cause the area of the ellipses to be substantially smaller. This is because, as the length of the high-pass median filter decreases, more of the low-frequency variability is removed. Therefore, at altitudes above the surface layer, we see a substantial difference between the areas contained by isopleths of CFs from data that had 20- and 60-point high-pass median filters applied. However, only a very small difference is seen in the areas from data that had the 50- and 60-point high-pass median filters applied. This indicates that most of the variability in the data occurs on scales smaller than about 50 points (750 m). Therefore, a 60-point (900 m) high-pass median filter was applied to the lidar data before CFs were computed. At all altitudes, the shape of the isopleths are approximately the same, indicating that ellipticity and orientation are insensitive to the choice of the median-filter length.

f. Effect of interpolation

For ease in data processing, all of the lidar data were converted from their original spherical coordinate sys-
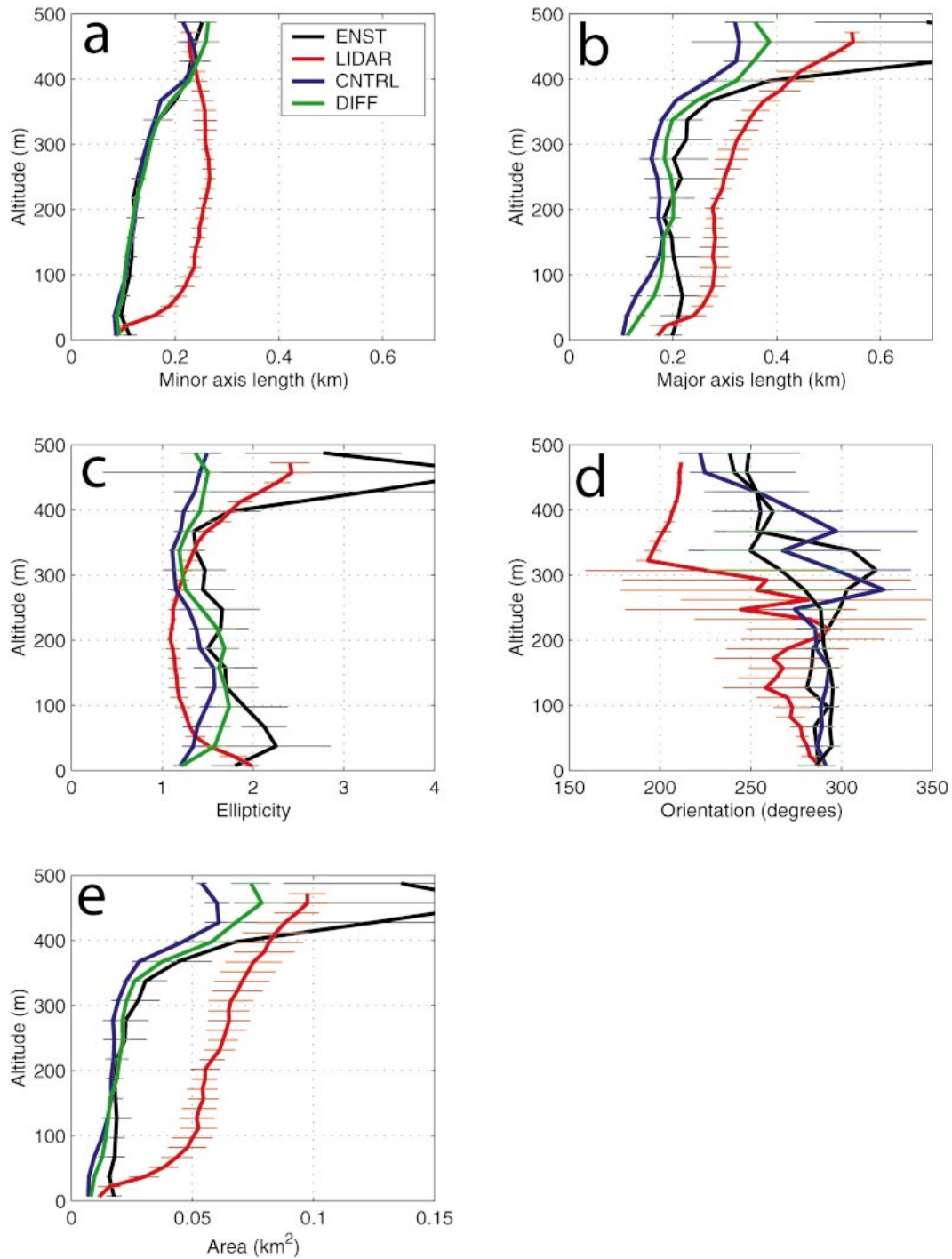
FIG. 17. Comparison of ellipse parameters averaged over offshore distances between 2.85 and 4.29 km. The red line is from RHI volume scan observations between 1719 and 1837 UTC and the other lines are from LES output as indicated in the legend of the upper-right panel.

tem (azimuth, elevation, and range) to a Cartesian co-ordinate system. Because the lidar beams are much farther apart at greater ranges, Cartesian grid elements, which have uniform spacing, are influenced by the same

data points and, therefore, cause correlation among the gridded data. For example, if there were no correlation between the gridded values (i.e., uncorrelated white noise), the CF would be a delta function. That is, it
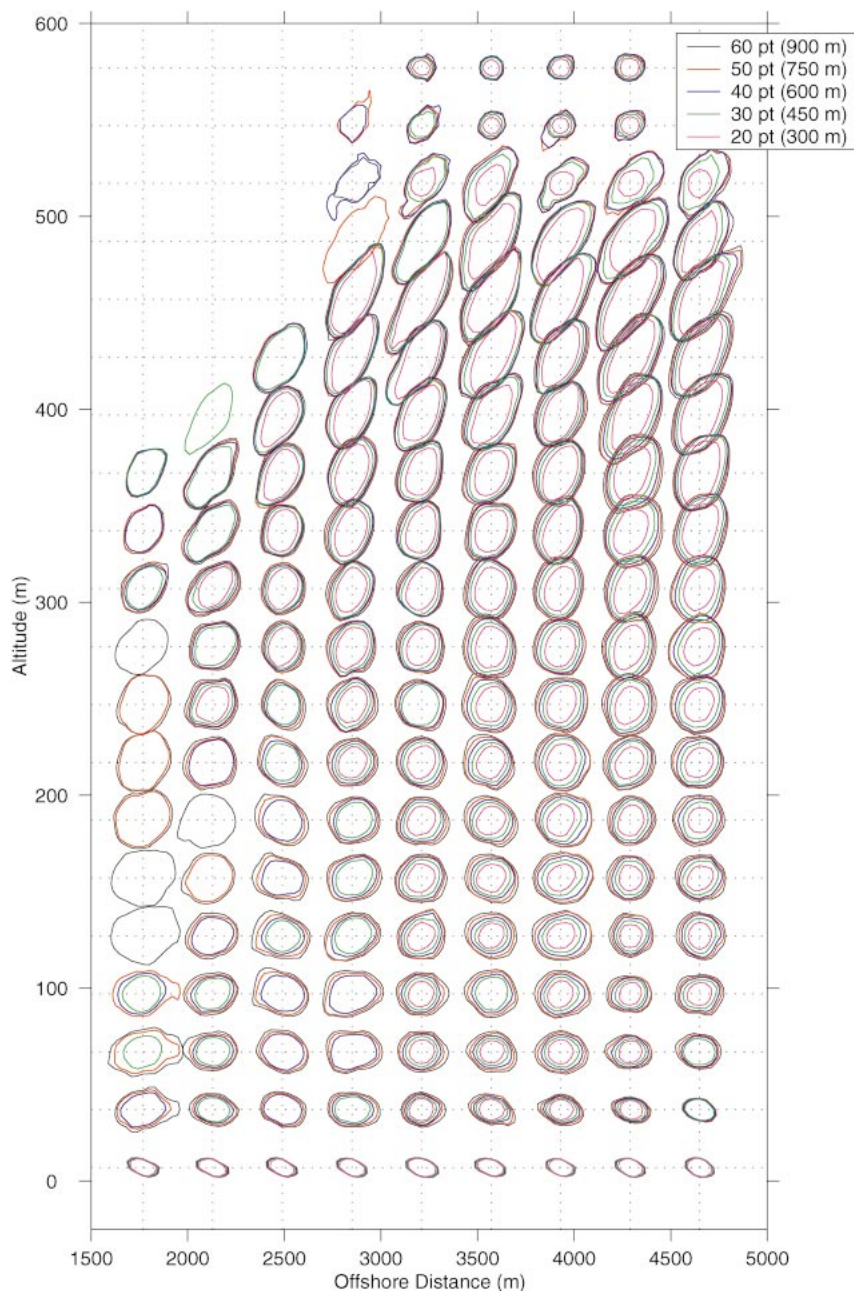
FIG. 18. Comparison of the 0.30 isopleth of correlation for CFs of RHI volume scan data on 13 Jan 1998 using five different high-pass median filter lengths. The inner contours correspond to the smaller filter lengths.

would equal one at the origin and be near zero for all other lags.

To examine the correlating effect of the gridding, CFs from lidar data above the boundary layer can be used. In this region, because of the absence of aerosol structures, the high-frequency information should be white and the CF should be a delta function. Figure 19 shows cross sections of CFs for three offshore distances: 3.2, 6.1, and 8.6 km. The cross sections broaden with increasing offshore distance, indicating that the interpolation does have an effect on the CF for lags smaller than about 150 m. This correlating effect increases as a function of offshore distance. Fortunately, the isopleths of correlation in the boundary layer for values greater than about 0.3 are farther away from the origin. Therefore, the effects of lidar data interpolation do not appear to significantly affect the observed ellipse parameters.
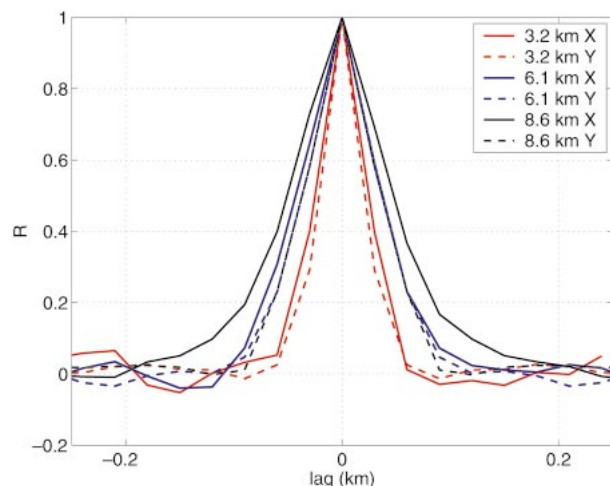
FIG. 19. East–west (solid) and north–south (dashed) cross sections of CFs for 3.2, 6.1, and 8.6 km offshore at 577 m altitude on 11 Jan 1998. This shows the correlating effect of placing the spherical coordinate lidar data onto an evenly spaced Cartesian grid.

g. CF sensitivity to optical scattering function

As we pointed out in section 3, the composition of atmospheric aerosols is quite variable, especially regionally, and, therefore, the sensitivity of optical scattering to increases in relative humidity change with time and location. To test the sensitivity of the CFs on a different optical scattering function, 2D CFs were recomputed for ENST using data obtained in Denver, Colorado, on 21 October 1971, by Covert et al. (1972). The best-fit function to the data is Eq. (2) and is shown as the dashed line in Fig. 5. Because of its midcontinental origin, this function is probably closer to the Sheboygan scattering function over a broad range of relative humidities.

The results of the comparison are shown in Figs. 20 and 21. They show that although the areas of the ellipses can be quite different, the orientations and ellipticities are very similar and that the exact function is not important for determining these two important eddy structure quantitites. The ellipses from LES output using the Covert et al. (1972) function are smaller in area because of the much higher range in scattering at high relative humidities. This results in a larger variance of the simulated lidar scattering.

6. Eddy lifetime from PPI scans

Thus far, we have emphasized the unique spatial imaging capability of the volume imaging lidar. However, the VIL is also capable of showing how the spatial patterns advect and decorrelate with *time*. In fact, it is the VIL's ability to measure the aerosol structure with sufficient *temporal* resolution that allowed the determination of aerosol motion as described by ME.

The following results were computed before the LES perturbation recycler was implemented. Therefore, we
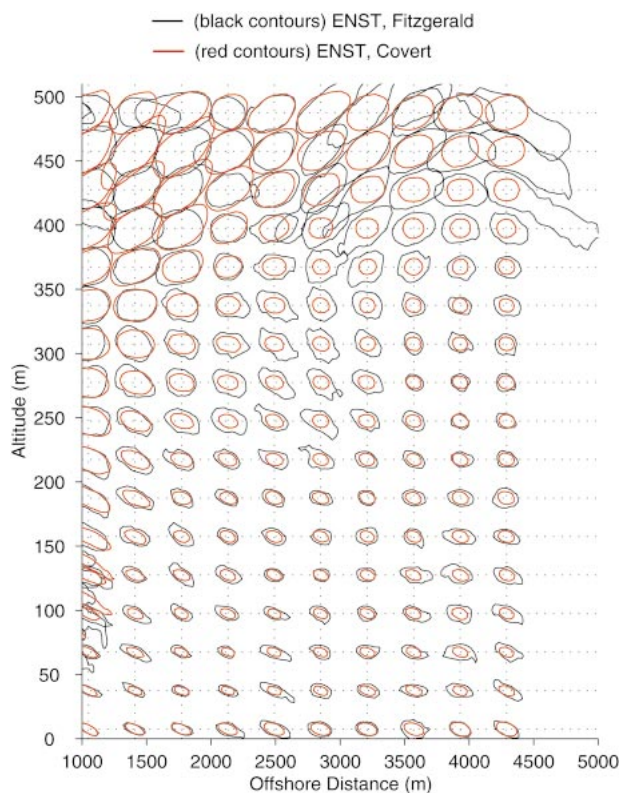

FIG. 20. Comparison of the 0.30 isopleths of correlation for CFs from ENST using optical scattering functions from Fitzgerald et al. (1982) (black) and Covert et al. (1972) (red).

use output from simulations where the turbulence was not as mature at the shoreline as in the simulations that did use the perturbation recycler. Our objective, as in previous sections, is to use the lidar data to judge which of the two simulations produced more realistic turbulence structures in terms of temporal correlation. We chose to make this evaluation for an altitude of 7.5 m and an offshore distance of 1800 m. One simulation used the Sadourny (1975) advection scheme and the other used a modified Arakawa and Lamb (1981) advection scheme.

Figure 22 shows examples of two-dimensional correlation functions for aerosol backscatter images separated by increasing amounts of time. The top pair of panels shows the correlation for zero time separation and so the peak is equal to one at the origin. The subsequent pairs of panels show the CFs from images with 24, 48, and 72 s of time separation, respectively. The peak moves downstream (along the white dashed line in the images in the left-hand column) due to the advection of coherent structures with the mean horizontal flow. The amplitudes of the peaks decrease with increasing time separation due mainly to the decorrelating effect of turbulence, although a random error inherent in the measurement is always present. To determine the amount of random noise in our data, we computed the
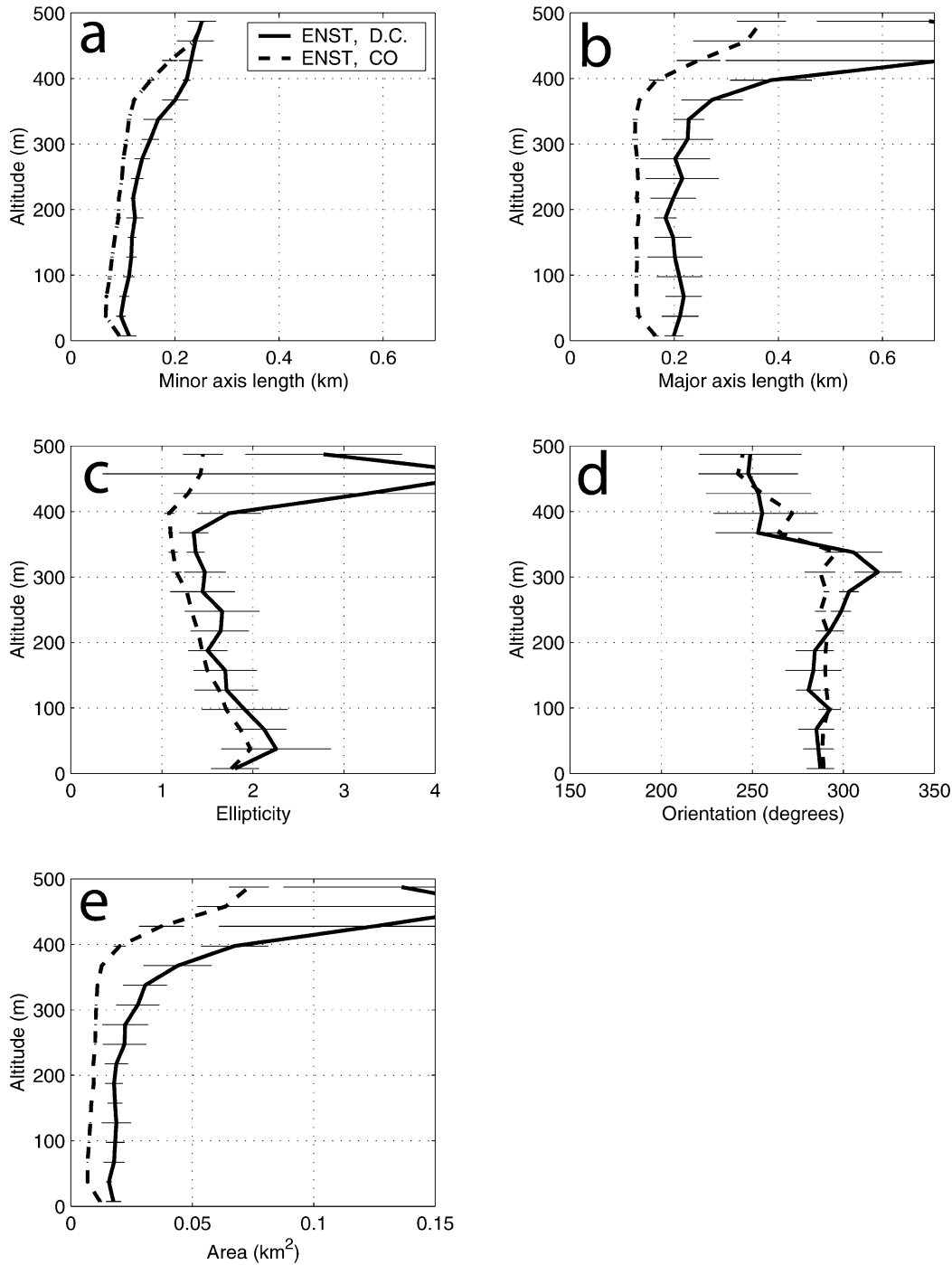
FIG. 21. Comparison of ellipse parameters from CFs of simulated lidar scattering on horizontal planes using output from ENST. The solid line is based on data collected by Fitzgerald et al. (1982) and the dashed line is based on data collected by Covert et al. (1972).

correlation coefficient between pairs of backscatter mea-surements separated in time by 0.01 s while the laser beam was stationary between PPI scan directions. When averaged over a range from 1 to 5 km offshore, the

correlation coefficient was 0.966. Therefore, the effect of noise in the measurement is negligible.

Figure 23a shows the CFs from lidar data interpolated to a line that runs through the origin and is parallel to
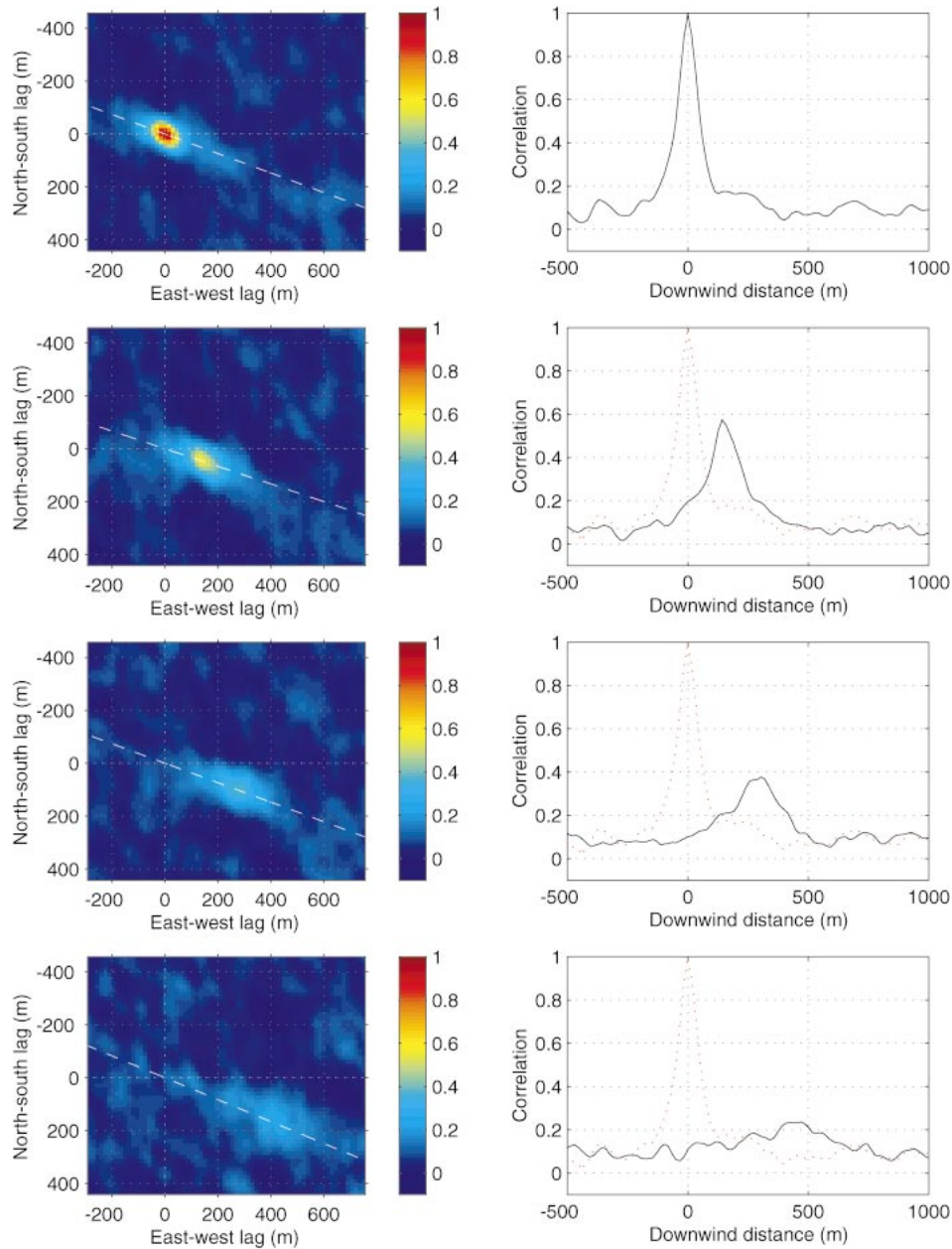
FIG. 22. Examples of 2D CFs from aerosol backscatter images separated in time. The time separation is 0, 24, 48, and 72 s from top to bottom.

the wind direction. Figure 23b shows the same result for the simulation that used the Sadourny advection scheme. The curves in Fig. 23c are from the run that used a modified Arakawa and Lamb advection scheme. To obtain the temporal decorrelation curves plotted in Fig. 24, the distances of the peaks in Figs. 23a–c were divided by their respective mean wind speed. For the lidar curve in Fig. 24, the correlation values for lags greater than zero were divided by 0.966 to compensate for the random measurement error. Figure 24 shows that the temporal decorrelation of the atmosphere for our

case was greater than either simulation and that the simulation using the modified Arakawa and Lamb advection scheme was closer to the observations than that which used the Sadourny advection scheme.

7. Conclusions

Unlike verifications for mesoscale and synoptic-scale model forecasts, which often include determining errors on the position and intensity of individual flow features, LES requires statistical verification. Until recently, the
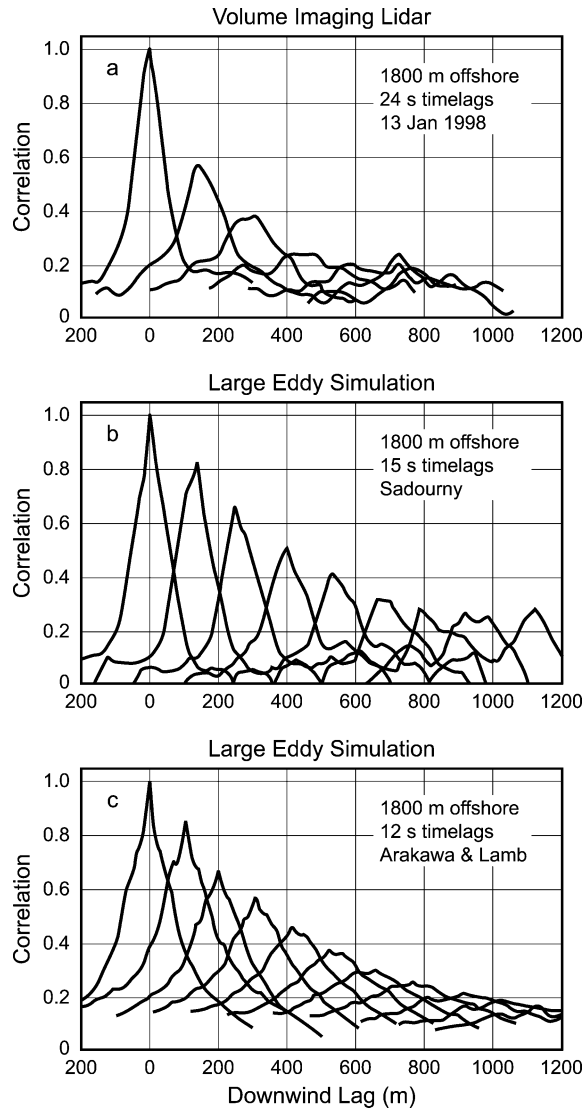
FIG. 23. The CFs interpolated along a line through the origin and parallel to the wind direction for increasing amounts of time separation for (a) lidar PPI scans, (b) LES using the Sadourny advection scheme, and (c) LES using the Arakawa and Lamb advection scheme.
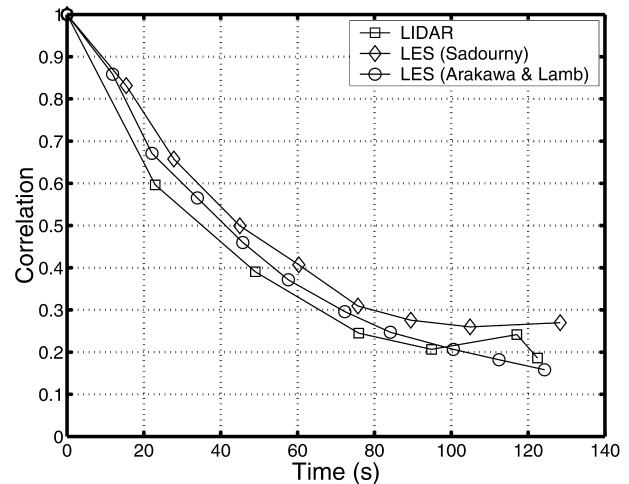

FIG. 24. Temporal correlation functions for the observations and two LES runs. These curves were obtained by dividing position of peaks in Fig. 23 by wind speed.

observational turbulence statistics were largely obtained from in situ sensors. Unfortunately, the use of in situ measurements restricts the spatial sampling to either a fixed point or line in space. Furthermore, to reduce sampling errors, such observations encouraged the study of homogeneous and stationary turbulent flows. Experiments using arrays of in situ sensors are severely limited in the spatial scales they can cover. Scanning radar and lidar data, however, provide two-, three-, and four-dimensional observations that reduce sampling errors and encourage the exploration of inhomogeneous and non-stationary flows. The comparisons we described should be done in addition to traditional LES tests.

Most of the work we presented here involved the demonstration of new methodologies that facilitate the comparison of observed and simulated eddy structure. This required the application of high-pass median filters to the lidar data and interpolation to Cartesian grids. We showed that a median filter can be applied to the lidar data without introducing biases as long as the filter length is larger than the mixed-layer depth. We also determined that the correlating effect of the interpolated data is confined to the first few lags near the origin. Most importantly, however, we found it necessary to create a functional relationship between model-predicted variables of relative humidity, a passive tracer, liquid water, and optical scattering to enable direct comparison of the observed and simulated eddy structure. Because of its vital role to this work, we tested two alternative functions currently available in the literature. Results showed ellipticity and orientation of model-predicted structures was insensitive to the particular function used, while the area enclosed by a given closed contour was sensitive. As a result, we concluded the area enclosed by a CF should not be used to compare LES to lidar, while orientation and ellipicity were deemed relevant and useful.

In addition to eddy structure, we demonstrated several other ways the four-dimensional lidar observations can be used to make direct qualitative and quantitative evaluations of the LES. We summarize key observations that were used to evaluate our LES solutions:

1) *VIL observations of turbulence structure at the shore* indicated that the boundary layer was continuously well mixed before it reached the shore on the day of interest. Prior to the lidar observations, our experimental design for Lake-ICE was to focus on the development of an unstable IBL over the lake within a preexisting stable boundary layer moving off the cold nocturnal snow-covered land. However, RHI scans normal to the shore clearly showed a turbulent

boundary layer advecting offshore. This not only confirmed the radiosonde observations of a 400-m-deep neutral layer over land, but it also demonstrated how this was important to the formation of turbulence structures as the flow moved offshore. We concluded that a simulation of the weakly convective land BL was necessary to capture the correct transition to a highly convective BL over the lake.

2) *VIL observations showed that the aerosol structures advected downstream and decorrelated with time.* Some of our first LES tests showed very well-organized, linear coherent structures that evolved very slowly and did not decorrelate with time. This clearly showed that the simulated structures were not consistent with the observed turbulent characteristics and so we needed to improve our turbulence representation by adjustment of the parameterization constants.

3) *VIL-derived wind vectors were used to evaluate how well the LES simulated mean acceleration and veering of the flow.* All three simulations produced too rapid a speed increase and two of the three simulations did not veer the wind.

4) *VIL observations revealed that the vertical variation of eddy structure was much larger than the horizontal variation.* Open-cell structure was observed near the surface and closed-cell structure above 100-m altitude, and both of these characteristics were observed at all offshore distances. Near the surface, there is a tendency for the small scales to be aligned parallel to the wind direction. Near the entrainment zone, the plumes tend to align in rows perpendicular to the mean flow, suggesting the organization is dominated by the influence of gravity waves in the inversion. The model also showed many of these characteristics; however, the ability to represent the open-cell character near the surface was dependent on the proper choice of nondimensional mixing coefficient.

5) *Comparison of lidar and model CFs suggests the model has a tendency to create more linear wind-parallel structures at all altitudes.* This could possibly be attributed to numerical phase dispersion, effectively smearing a structure in the direction of the flow. Another possible cause is the inability of the model to generate sufficient wave activity due to the limited domain height and hard upwind boundary condition.

6) *VIL observations of convective plumes above the surface layer and within 3 km of the shore tended to be organized into linear bands perpendicular to the flow.* This pattern, detected at long lags in the CF, was not represented in the LES that, instead, contained wind-parallel roll-like structures. This demonstrated a much more dominant role of gravity waves in the VIL observations than was represented in the LES. As we discuss, the experimental design of the LES, based on suppressing gravity waves and their influence in the boundary layer, was flawed.

Ironically, this study shows that the model generates reasonable coherent structures (open cells) where it was expected to perform poorly (the lowest grid point) and fails to capture the wind-perpendicular organization of closed cells in the middle of the mixed layer where the LES technique is expected to be robust. This points to the importance of boundary conditions and gravity waves when attempting to simulate real atmospheric boundary layers.

APPENDIX

Method Used to Compute 2D Correlation Functions

For two-dimensional (2D) data that are homogeneous in both directions, 2D autocorrelation functions (ACFs) can be computed using fast Fourier transforms (FFTs) or by incrementally shifting an image with respect to itself and computing a correlation coefficient for each pair of lags. For horizontally homogeneous data, the resulting ACF is representative of the properties at any position in the images used to compute it. In this work, because of the inhomogeneity of the boundary layer in the east–west direction, a slightly different procedure was used. Here, correlation coefficients are calculated only for north–south-oriented one-dimensional arrays. It is assumed that the turbulence statistics are homogeneous only in the shore-parallel direction. The 2D CF, therefore, was computed using the linear-correlation coefficient for shifted north–south-oriented rows of data at the same altitude. Here, the amount of east–west shift is called the x lag and the amount of north–south shift is called the y lag. Lags to the east and north are positive lags. Figure A1 illustrates how the shifted arrays, a and b, are extracted from a 2D grid of data points for a single pair of lags. The 2D cross-correlation functions (CFs) were computed from data on horizontal planes at a series of offshore distances. The RHI volume scan data enabled this to be done at multiple altitudes.

The formula for the linear correlation coefficient (Bevington 1969) is

$$R = \frac{N \sum a_i b_i - \sum a_i \sum b_i}{\left[N \sum a_i^2 - \left(\sum a_i\right)^2\right]^{1/2}\left[N \sum b_i^2 - \left(\sum b_i\right)^2\right]^{1/2}}.$$
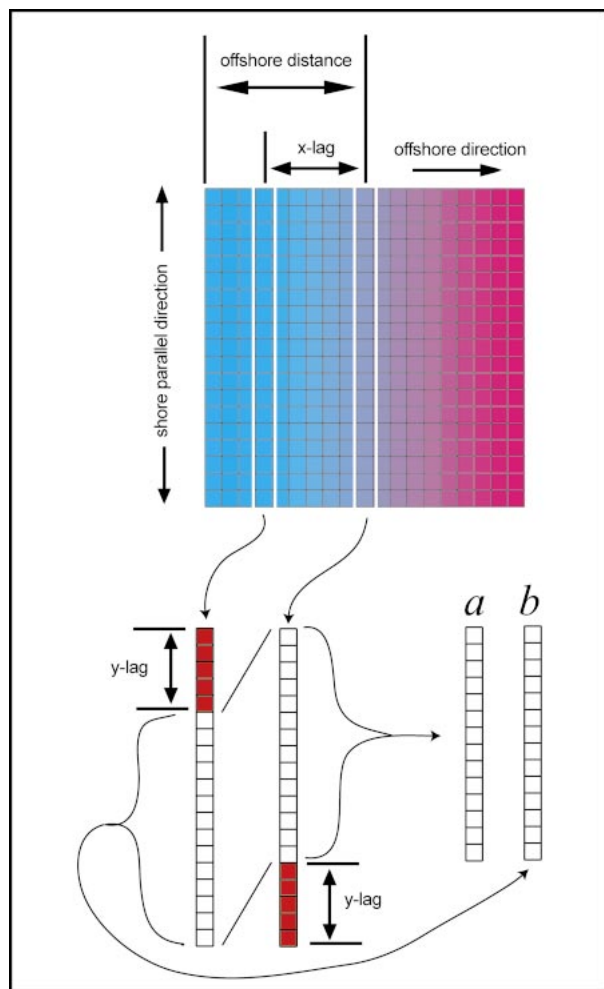
$$(A1)$$

FIG. A1. Illustration showing how shifted arrays are extracted from gridded data that are inhomogeneous in the *x* direction. The linear correlation coefficient will be computed from (a) and (b) for the given *x* and *y* lag.

FIG. A2. (top) The 3D view of a CF for lags ±200 m from the origin. (bottom) The 2D view of the same CF with a 0.3 contour drawn for example.

Here, *a* and *b* are the shifted north–south-oriented arrays and *i* is the index into either array; *N* is the number of points in either the *a* or *b* array. Because the azimuthal limits of the lidar scans usually do not line up with the cardinal directions, parts of the gridded data are usually filled with values to indicate an absence of data. If a "no data" flag is present in either *a* or *b*, the companion value is changed to a no data flag and that pair is not used in the calculation of the correlation coefficient. Correlation coefficients were only calculated if at least 20 data pairs were available for any lag. If 20 pairs were not available, the 2D CF was marked with the no data flag at that *x*-lag and *y*-lag locations. Figure A2 shows an example of one CF from 3D and 2D perspectives.

It should be noted that Eq. (A1) produces an illegal arithmetic operation when the denominator is zero. This occurs if either the *a* or *b* array is filled with a constant value. Unfortunately, the lidar data and LES output occasionally have short segments of constant values. In
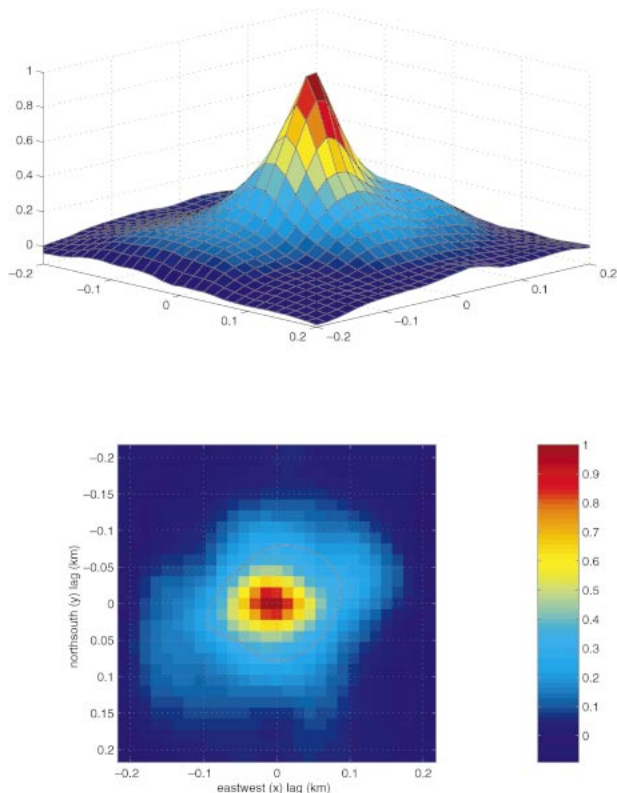
the lidar data, the constant values are caused when fluctuations in scattering are smaller than the digital resolution of the analog-to-digital converter. Because a log amplifier is used, the values occur when the aerosol scattering is homogeneous at close ranges. Constant values occur in the simulated lidar backscatter because the crude algorithm used to compute simulated lidar backscatter from model output sets the scattering to a constant value when any amount of liquid water is present at a grid point. The solution to this problem in the present work was to check every *a* and *b* array for constant values before using them in Eq. (A1). If either *a* or *b* contained a majority of constant values, then the correlation function was marked with a no data flag for that particular set of lags.

REFERENCES

Andren, A., A. R. Brown, J. Graf, P. J. Mason, C.-H. Moeng, F. T. M. Nieuwstadt, and U. Schumann, 1994: Large-eddy simulation of a neutrally stratified boundary layer: A comparison of four computer codes. *Quart. J. Roy. Meteor. Soc.,* **120,** 1457–1484.

Arakawa, A., and V. R. Lamb, 1981: A potential enstrophy and energy conserving scheme for the shallow water equations. *Mon. Wea. Rev.,* **109,** 18–36.

Atkinson, B. W., and J. W. Zhang, 1996: Mesoscale shallow convection in the atmosphere. *Rev. Geophys.,* **34,** 403–431.

Avissar, R., E. W. Eloranta, K. Gurer, and G. J. Tripoli, 1998: An evaluation of the large-eddy simulation option of the regional atmospheric modeling system in simulating a convective boundary layer: A FIFE case study. *J. Atmos. Sci.,* **55,** 1109–1130.

Bevington, P. R., 1969: *Data Reduction and Error Analysis for the Physical Sciences.* McGraw-Hill, 336 pp.

Covert, D. S., R. J. Charlson, and N. C. Ahlquist, 1972: A study of the relationship of chemical composition and humidity to light scattering by aerosols. *J. Appl. Meteor.,* **11,** 968–976.

Eloranta, E. W., and D. K. Forrest, 1992: Volume-imaging lidar observations of the convective structure surrounding the flight path of a flux-measuring aircraft. *J. Geophys. Res.,* **97,** 18 383–18 393.

——, J. M. King, and J. A. Weinman, 1975: The determination of wind speeds in the boundary layer by monostatic lidar. *J. Appl. Meteor.,* **14,** 1485–1489.

Ferrare, R. A., E. W. Eloranta, and R. Coulter, 1991: Lidar observations of banded convection during BLX83. *J. Appl. Meteor.,* **30,** 312–326.

Fitzgerald, J. W., W. A. Hoppel, and M. A. Vietti, 1982: The size and scattering coefficient of urban aerosol particles at Washington, DC as a function of relative humidity. *J. Atmos. Sci.,* **39,** 1838–1852.

Gander, W., G. H. Golub, and R. Strebel, 1994: Fitting of circles and ellipses least squares solution. Tech. Rep. 217, Institut fur Wissenschaftliches Rechnen, Departement Informatik, ETH Zurich, Zurich, Switzerland, 57 pp.

Gluhovsky, A., and E. Agee, 1994: A definitive approach to turbulence statistical studies in planetary boundary layers. *J. Atmos. Sci.,* **51,** 1682–1690.

Hauf, T., and T. L. Clark, 1989: Three-dimensional numerical experiments on convectively forced internal gravity waves. *Quart. J. Roy. Meteor. Soc.,* **115,** 309–333.

Khanna, S., and J. G. Brasseur, 1997: Analysis of Monin–Obukhov similarity from large-eddy simulations. *J. Fluid Mech.,* **345,** 251–286.

Konrad, T. G., 1970: The dynamics of the convective process in clear air as seen by radar. *J. Atmos. Sci.,* **27,** 1138–1147.

Kristovich, D. A. R., and Coauthors, 2000: The Lake-Induced Convection Experiment and the Snowband Dynamics Project. *Bull. Amer. Meteor. Soc.,* **81,** 519–542.

Kunkel, K., 1978: Measurement of upper convective boundary layer parameters by means of lidar. Ph.D. thesis, University of Wisconsin—Madison, 129 pp.

——, E. W. Eloranta, and J. Weinman, 1980: Remote determination of winds, turbulence spectra and energy dissipation rates in the boundary layer from lidar measurements. *J. Atmos. Sci.,* **37,** 978–985.

Lenschow, D. H., J. Mann, and L. Kristensen, 1994: How long is long enough when measuring fluxes and other turbulence statistics? *J. Atmos. Oceanic Technol.,* **11,** 661–673.

Lund, T. S., X. Wu, and K. D. Squires, 1998: Generation of turbulent inflow data for spatially-developing boundary layer simulations. *J. Comput. Phys.,* **140,** 233–258.

Mason, P. J., 1989: Large-eddy simulation of the convective atmospheric boundary layer. *J. Atmos. Sci.,* **46,** 1492–1516.

Mayor, S. D., 2001: Volume imaging lidar observations and large-eddy simulations of convective internal boundary layers. Ph.D. thesis, University of Wisconsin—Madison, 177 pp.

——, and E. W. Eloranta, 2001: Two-dimensional vector wind fields from volume imaging lidar data. *J. Appl. Meteor.,* **40,** 1331–1346.

——, G. J. Tripoli, E. W. Eloranta, and B. Hoggatt, 1999: Comparison of microscale convection patterns seen in lidar data and large-eddy simulations. Preprints, *13th Symp. on Boundary Layers and Turbulence,* Dallas, TX, Amer. Meteor. Soc., 271–274.

——, P. R. Spalart, and G. J. Tripoli, 2002: Application of a perturbation recycling method to a large eddy simulation of a mesoscale convective internal boundary layer. *J. Atmos. Sci.,* **59,** 2385–2395.

Nieuwstadt, F. T. M., P. J. Mason, C.-H. Moeng, and U. Schumann, 1993: Large-eddy simulation of the convective boundary layer: A comparison of four computer codes. *Turbulent Shear Flows 8,* F. Friedrich, et al., Eds., Springer-Verlag, 343–367.

Porch, W. M., and D. A. Gillette, 1977: A comparison of aerosol and momentum mixing in dust storms using fast-response instruments. *J. Appl. Meteor.,* **16,** 1273–1281.

Sadourny, R., 1975: The dynamics of finite-difference models of the shallow-water equations. *J. Atmos. Sci.,* **32,** 680–689.

Sasano, Y., H. Hirohara, T. Yamasaki, H. Shimizu, N. Takeuchi, and T. Kawamura, 1982: Horizontal wind vector determination from the displacement of aerosol distribution patterns observed by a scanning lidar. *J. Appl. Meteor.,* **21,** 1516–1523.

Schmidt, H., and U. Schumann, 1989: Coherent structures of the convective boundary layer derived from large-eddy simulations. *J. Fluid Mech.,* **200,** 511–562.

Schols, J. L., and E. W. Eloranta, 1992: The calculation of area-averaged vertical profiles of the horizontal wind velocity from volume imaging lidar data. *J. Geophys. Res.,* **97,** 18 395–18 407.

Spalart, P. R., 1988: Direct simulation of a turbulent boundary layer up to $r_\theta = 1140$. *J. Fluid Mech.,* **187,** 61–98.

Stevens, B., and D. H. Lenschow, 2001: Observations, experiments, and large eddy simulations. *Bull. Amer. Meteor. Soc.,* **82,** 283–294.

Tripoli, G. J., 1992: A nonhydrostatic mesoscale model designed to simulate scale interaction. *Mon. Wea. Rev.,* **120,** 1342–1359.

Willis, G. E., and J. W. Deardorff, 1979: Laboratory observations of turbulent penetrative-convection planforms. *J. Geophys. Res.,* **84,** 295–302.